PAPER

Check for updates

Design, synthesis, anti-proliferative evaluation, docking, and MD simulation studies of new thieno [2,3-*d*]pyrimidines targeting VEGFR-2†

Souad A. El-Metwally,[a] Hazem Elkady, ✶[b] Mohamed Hagras,[c] Dalal Z. Husein,[d] Ibrahim M. Ibrahim,[e] Mohammed S. Taghour,[b] Hesham A. El-Mahdy,[f] Ahmed Ismail,[f] Bshra A. Alsfouk,[g] Eslam B. Elkaeed,[h] Ahmed M. Metwaly ✶[ij] and Ibrahim H. Eissa ✶[b]

In this work, new thieno[2,3-*d*]pyrimidine-derived compounds possessing potential anticancer activities were designed and synthesized to target VEGFR-2. The thieno[2,3-*d*]pyrimidine derivatives were tested *in vitro* for their abilities to inhibit VEGFR-2 and to prevent cancer cell growth in two types of cancer cells, MCF-7 and HepG2. Compound **18** exhibited the strongest anti-VEGFR-2 potential with an IC_{50} value of 0.084 μM. Additionally, it displayed excellent proliferative effects against MCF-7 and HepG2 cancer cell lines, with IC_{50} values of 10.17 μM and 24.47 μM, respectively. Further studies revealed that compound **18** induced cell cycle arrest in G2/M phase and promoted apoptosis in MCF-7 cancer cells. Apoptosis was stimulated by compound **18** by increasing BAX (3.6-fold) and decreasing Bcl-2 (3.1-fold). Additionally, compound **18** significantly raised the levels of caspase-8 (2.6-fold) and caspase-9 (5.4-fold). Computational techniques were also used to investigate the VEGFR-2-**18** complex at a molecular level. Molecular docking and molecular dynamics simulations were performed to assess the structural and energetic features of the complex. The protein-ligand interaction profiler analysis identified the 3D interactions and binding conformation of the VEGFR-2-**18** complex. Essential dynamics (ED) study utilizing principal component analysis (PCA) described the protein dynamics of the VEGFR-2-**18** complex at various spatial scales. Bi-dimensional projection analysis confirmed the proper binding of the VEGFR-2-**18** complex. In addition, the DFT studies provided insights into the structural and electronic properties of compound **18**. Finally, computational ADMET and toxicity studies were conducted to evaluate the potential of the thieno [2,3-*d*]pyrimidine derivatives for drug development. The results of the study suggested that compound **18** could be a promising anticancer agent that may provide effective treatment options for cancer patients. Furthermore, the computational techniques used in this research provided valuable insights into the molecular interactions of the VEGFR-2-**18** complex, which may guide future drug design efforts. Overall, this study highlights the potential of thieno[2,3-*d*]pyrimidine derivatives as a new class of anticancer agents and provides a foundation for further research in this area.

[a]Department of Basic Science, Higher Technological Institute, 10th of Ramadan City, Egypt

[b]Pharmaceutical Medicinal Chemistry & Drug Design Department, Faculty of Pharmacy (Boys), Al-Azhar University, Cairo, 11884, Egypt. E-mail: Ibrahimeissa@azhar.edu.eg; Hazemelkady@azhar.edu.eg

[c]Department of Pharmaceutical Organic Chemistry, College of Pharmacy (Boys), Al-Azhar University, Cairo 11884, Egypt

[d]Chemistry Department, Faculty of Science, New Valley University, El-Kharja 72511, Egypt

[e]Biophysics Department, Faculty of Science, Cairo University, Cairo 12613, Egypt

[f]Biochemistry and Molecular Biology Department, Faculty of Pharmacy (Boys), Al-Azhar University, Nasr City, Cairo 11231, Egypt

[g]Department of Pharmaceutical Sciences, College of Pharmacy, Princess Nourah bint Abdulrahman University, P.O. Box 84428, Riyadh 11671, Saudi Arabia

[h]Department of Pharmaceutical Sciences, College of Pharmacy, AlMaarefa University, Riyadh 13713, Saudi Arabia

[i]Pharmacognosy and Medicinal Plants Department, Faculty of Pharmacy (Boys), Al-Azhar University, Cairo 11884, Egypt. E-mail: ametwaly@azhar.edu.eg

[j]Biopharmaceutical Products Research Department, Genetic Engineering and Biotechnology Research Institute, City of Scientific Research and Technological Applications (SRTA-City), Alexandria, Egypt

† Electronic supplementary information (ESI) available. See DOI: https://doi.org/10.1039/d3ra03128d

1.   Introduction

The discovery of effective treatments for cancer is a multifaceted challenge that demands a comprehensive understanding of the underlying biological mechanisms responsible for the disease's onset and progression.[1] As such, cancer therapy continues to be an active field of research, with investigators diligently striving to develop novel therapies that can optimize patient outcomes and ultimately diminish the incidence of cancer.[2]

Receptor tyrosine kinases are a class of protein kinases that govern inter- and intracellular signaling *via* signal transduction pathways.[3] These proteins play a significant role in the regulation of cellular processes such as growth, proliferation, differentiation, survival, and metabolism.[4] Among these, vascular endothelial growth factor receptor-2 (VEGFR-2) is a crucial mediator of endothelial cell migration and proliferation.[5] In the context of cancer cells, VEGFR-2 has been identified as a principal driver of cancer cell proliferation, migration, and angiogenesis.[6] Additionally, it has been identified through scientific inquiry that a significant upregulation of VEGFR-2 expression is present in a wide range of cancer types.[7] Therefore, VEGFR-2 represents a major therapeutic target for the inhibition of cancer growth and metastasis, given its pivotal function in angiogenesis regulation.[8]

Our laboratory has discovered a plethora of prospective anticancer agents that exhibit inhibitory activity towards VEGFR-2. These agents stem from diverse classes and derivatives, encompassing nicotinamide,[9–11] thiazolidine,[12,13] naphthalene,[14] pyridine,[15] quinoline,[16] indole,[17] and isatin.[18]
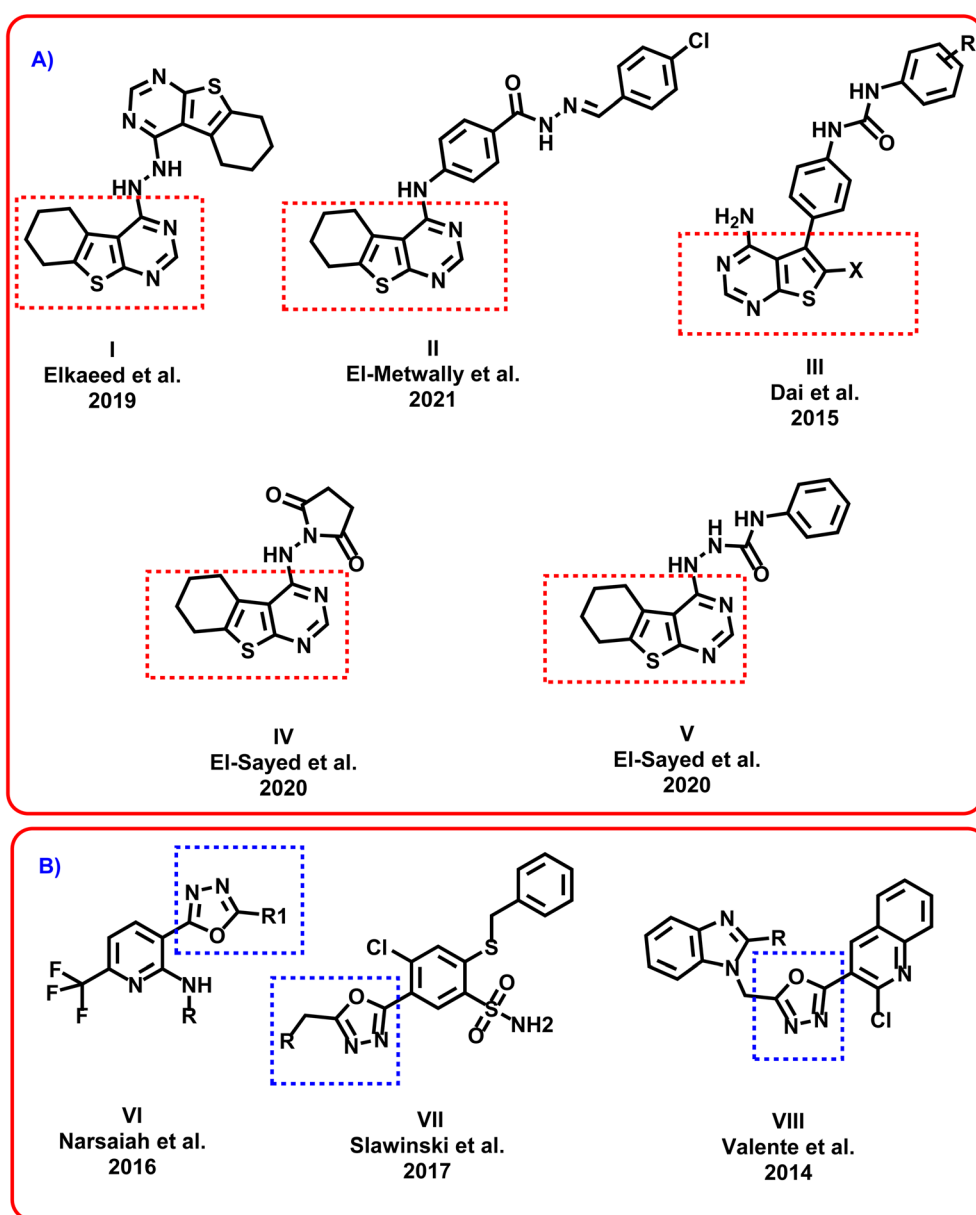

Fig. 1   (A) Reported thieno[2,3-*d*]pyrimidin-4(3*H*)-one derivatives as anticancer agents. (B) Reported 1,3,4-oxadiazol derivatives as promising anticancer agents.

1.1. Rationale

Thieno[2,3-d]pyrimidin-4(3H)-one is a privileged scaffold that exhibited a high interest due to its wide variety of biological effects.[19] Thieno[2,3-d]pyrimidin-4(3H)-one shows a broad anticancer activity directing different vital biological targets.[20] Moreover, thieno[2,3-d]pyrimidin-4(3H)-one has been utilized as a core scaffold for the design and synthesis of many tyrosine kinase inhibitors.[21] Elkaeed *et al.* reported compound **I** as promising anticancer agent targeting EGFR.[22] El-Metwally *et al.* designed and synthesized compound **II** which exhibited promising VEGFR-2 inhibitory activity.[23] Dai *et al.* introduced compound **III** as good a series of thienopyrimidine-based receptor tyrosine kinase inhibitors that potently inhibited VEGF and PDGF receptor tyrosine kinases.[24] El-Sayed *et al.* discovered compounds **IV** and **V** as potential inhibitors of topoisomerase **II** (ref. 25) (Fig. 1).

Additionally, a considerable attention has been paid to the 1,3,4-oxadiazol moiety. It was emerged in many bioactive agents.[26] A wide number of 1,3,4-oxadiazole derivatives showed potent anticancer effects.[27] Narsaiah *et al.* synthesized a new series of 1,3,4-oxadiazol derivatives **VI** which showed promising cytotoxicity against HeLa, DU145, HepG2, and MBA-MB-231, cancer cell lines.[28] Slawinski *et al.* designed and synthesized series **VII** as potential antitumor agents against colon cancer, breast cancer, and cervical cancer.[29] Valente *et al.* discovered compound **VIII** as promising anticancer agent against leukemia cells[30] (Fig. 1).

The ATP-binding site is occupied by VEGFR-2 inhibitors which should have four pharmacophoric features (Fig. 2A).[31–33] These features are a hetero aromatic system, a spacer moiety, pharmacophore moiety (HBD/HBA), and hydrophobic tail to occupy the hinge region,[32] the linker region,[34] the DFG motif,[35] the allosteric pocket,[36] respectively.
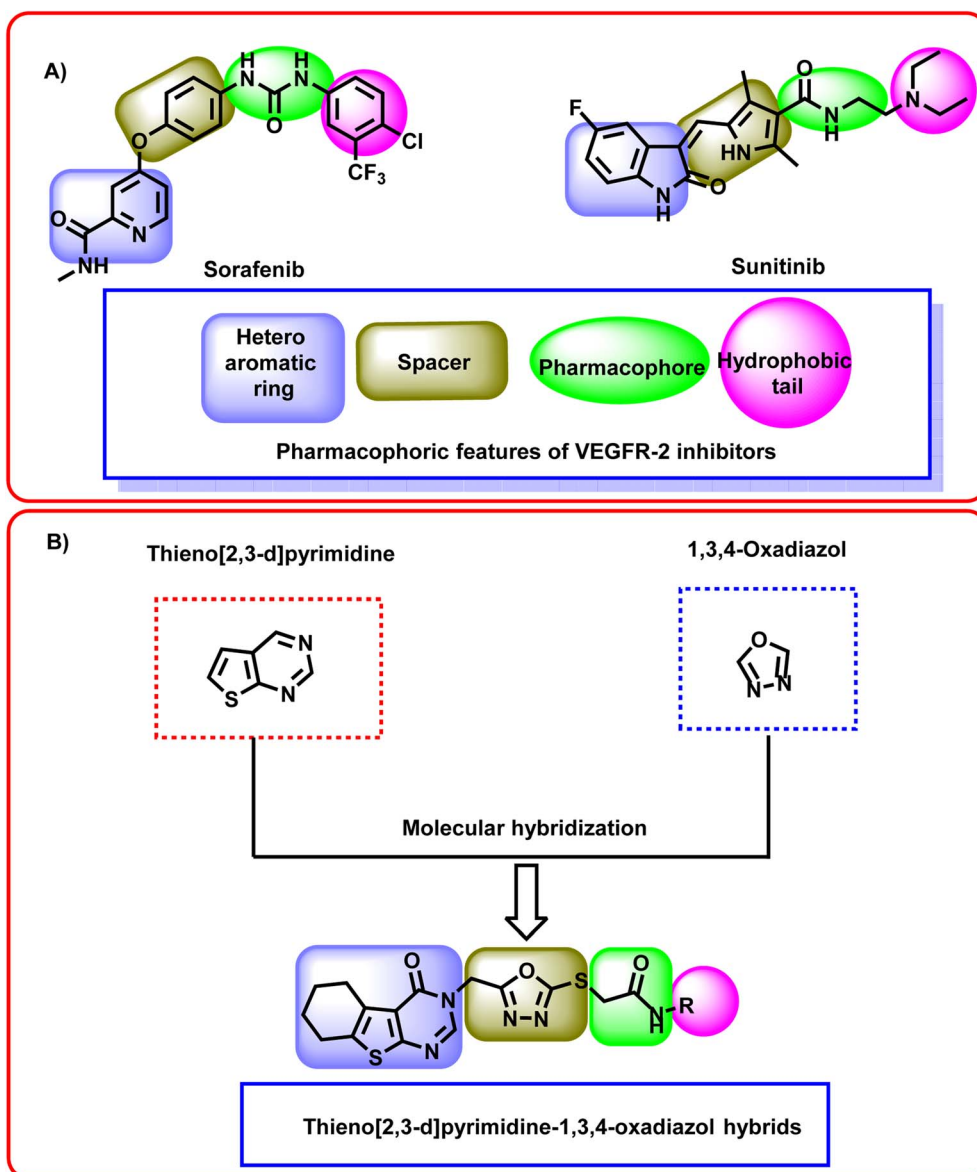

Fig. 2 (A) Some reported VEGFR-2 inhibitors showing the essential pharmacophoric features. (B) The hybridization strategy of molecular design.

In this study, a molecular hybridization strategy was applied between thieno[2,3-*d*]pyrimidin-4(3*H*)-one and 1,3,4-oxadiazol moieties to reach a new series of VEGFR-2 inhibitors. In which the thieno[2,3-*d*]pyrimidin-4(3*H*)-one was used as a hetero aromatic system to occupy the hinge region. 1,3,4-Oxadiazol moiety was used as a spacer moiety to occupy the linker region. The amide moiety was used as a pharmacophore group to occupy the DFG motif region. Finally, different hydrophobic moieties were utilized as a hydrophobic tail to occupy the allosteric binding pocket (Fig. 2B).

2.   Results and discussion

2.1.   Chemistry

The synthetic itineraries for preparation of the target candidates **18–22** were fully illustrated in Schemes 1–3. According to the reported processes, the starting materials **1** (ref. 37) and

2 (ref. 38) were produced in excellent yields. Then, compound **2** was heated with a potassium hydroxide in absolute ethanol to produce the potassium salt **3**. The ester derivative **4** was furnished by refluxing the potassium salt **3** and ethyl chloroacetate in the DMF/KI mixture.[39] This ester derivative then reacted with hydrazine hydrate to create the acid hydrazide **5**.[40] The 5-mercapto-1,3,4-oxadiazole derivative **6** (ref. 40) was obtained *via* refluxing of acid hydrazide **5** with the clear yellow solution of CS$_2$/KOH in ethanol followed by acidification with HCl. The key starting material **7** was prepared in the present work by refluxing compound **6** with alcoholic KOH while continuous stirring (Scheme 1).

Alternatively, chloroacetyl chloride was dropped onto different solutions of DMF each containing the proper amine namely piperidine (**8**), 2,6-dinitroaniline (**9**), 5-chloropyridin-2-amine (**10**), thiazol-2-amine (**11**), and benzo[*d*]thiazol-2-amine (**12**) to produce the corresponding acetamide derivatives
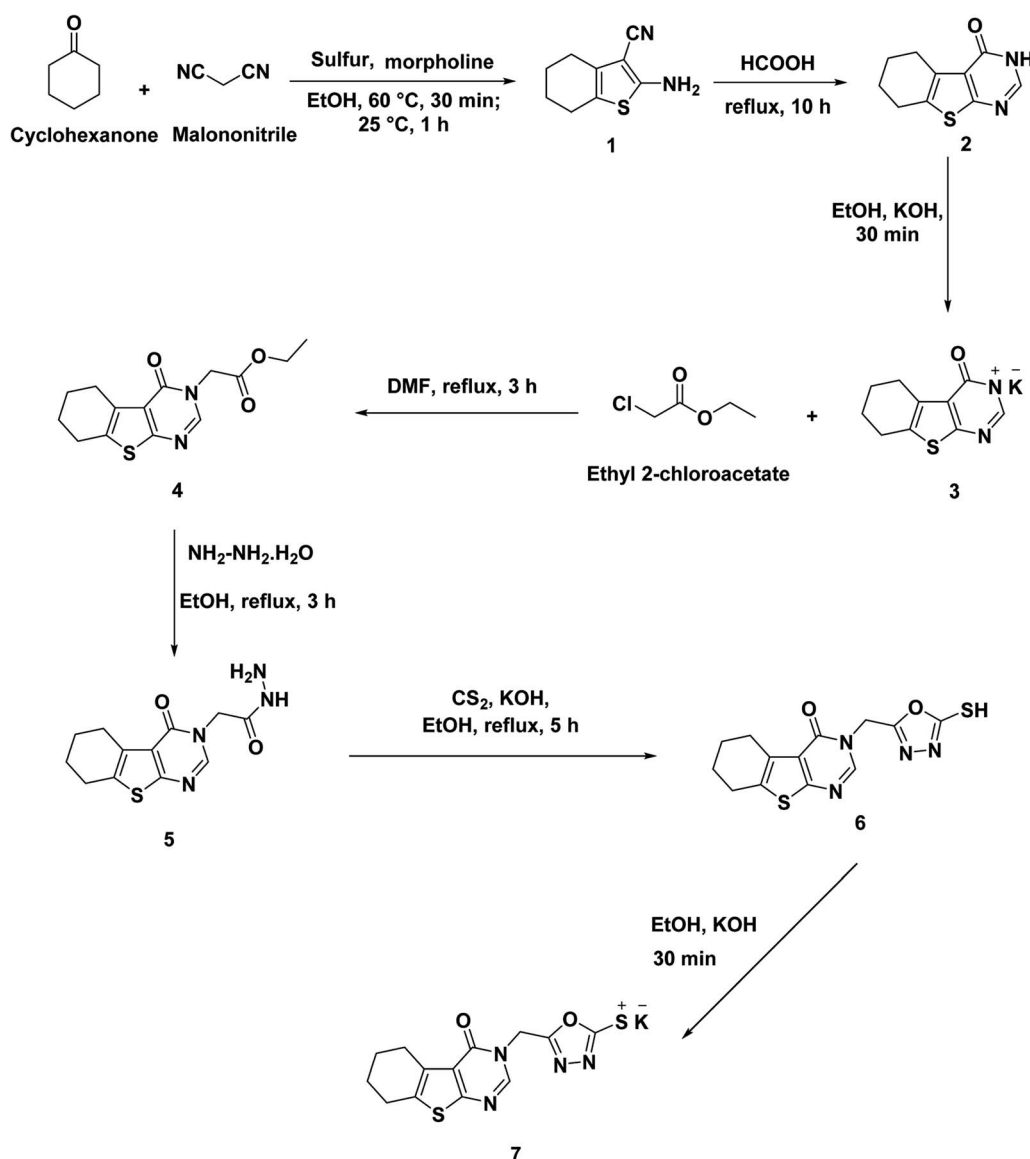
Scheme 1 Synthesis of the key starting material **7**.
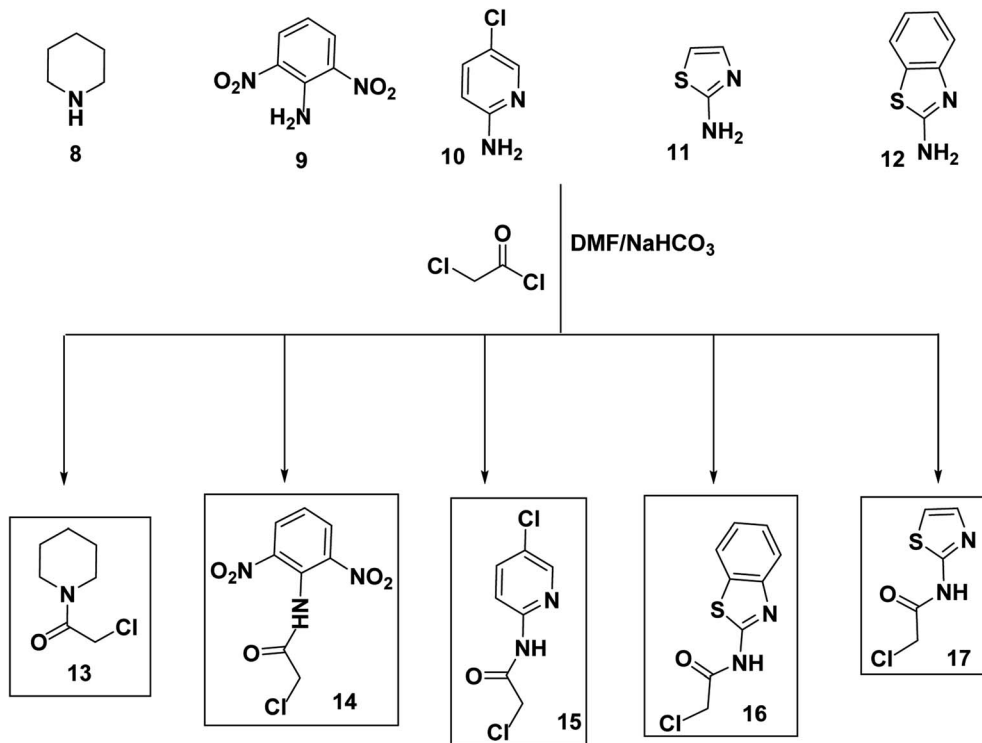
Scheme 2 Synthesis of the key intermediates **13–17**.

namely, 2-chloro-1-(piperidin-1-yl)ethan-1-one (**13**), 2-chloro-*N*-(2,6-dinitrophenyl)acetamide (**14**), 2-chloro-*N*-(5-chloropyridin-2-yl)acetamide (**15**), *N*-(benzo[*d*]thiazol-2-yl)-2-chloroacetamide (**16**), and 2-chloro-*N*-(thiazol-2-yl)acetamide (**17**) (Scheme 2).

As a final point, compound **7** was heated with the appropriate acetamide derivatives **13–17** in DMF mixtures comprising catalytic KI to produce the final target derivatives **18–22**, respectively (Scheme 3).

The IR spectra of the final candidates exhibited the appearance of absorption bands at the ranges of 3291–3400 cm^{-1} and 1661–1674 cm^{-1} due to the NH and C=O groups, respectively. In addition, ^{1}H NMR analyses showed singlet signal appeared at around δ 8.44 ppm corresponding to the pyrimidine proton besides characteristic signals for additional aromatic and aliphatic protons. Taken compound **18** as representative example, it showed many characteristic signals at aliphatic region corresponding to the piperidine moiety. Moreover, ^{13}C NMR spectra of such compound confirmed the previous results as the aliphatic protons of appeared at the aliphatic region.

2.2. Biological investigations

2.2.1. *In vitro* cytotoxicity. The present investigation aimed to explore the anti-proliferative activities of the obtained thieno[2,3-*d*]pyrimidine derivatives against HepG2 and MCF-7 tumor cell lines, using the MTT assay[41] against sorafenib as a positive control. The results presented in Table 1 showed that the tested members displayed powerful cytotoxic effects against MCF-7 and HepG2 cells with IC$_{50}$ values

ranging from 4.84 to 24.27 µM, comparing to those of sorafenib (IC$_{50}$ = 9.98 and 13.26 µM against MCF-7 and HepG2 cells, respectively).

In details, compounds **20** showed the highest anti-proliferative activities with IC$_{50}$ values of 5.38 and 4.84 µM against MCF-7 and HepG2 cells, respectively. In addition, compounds **21** (IC$_{50}$ = 6.31 and 11.83 µM) and **22** (IC$_{50}$ = 5.73 and 5.51 µM) showed strong anti-proliferative activities against MCF-7 and HepG2 cells, respectively. For compounds **18** (IC$_{50}$ = 10.17 and 24.27 µM) and **19** (IC$_{50}$ = 16.50 and 31.78 µM) showed moderate anti-proliferative activities against MCF-7 and HepG2 cells, respectively.

2.2.2. *In vitro* VEGFR-2 inhibitory activity. Additionally, the study evaluated the prepared thieno[2,3-*d*]pyrimidine derivatives for their inhibitory effects on VEGFR-2, with sorafenib used as the reference drug. The findings revealed that compound **18** exhibited a promising IC$_{50}$ value of 0.18 µM, suggesting its potential as an anti-angiogenic agent. As compound **18** was the most potent inhibitor, further investigations are warranted to validate its efficacy and safety of as an anticancer agent.

2.2.3. Flow cytometry. The revolutionary technique of flow cytometry has made it possible to identify various cell populations at different stages of the cell cycle, including G0/G1, S, and G2/M.[42] This application of flow cytometry is critical for researchers to gain insights into the mechanisms that regulate cell proliferation and differentiation.[43] Moreover, flow cytometry allows researchers to pinpoint the growth stages affected by anticancer drugs, providing valuable information
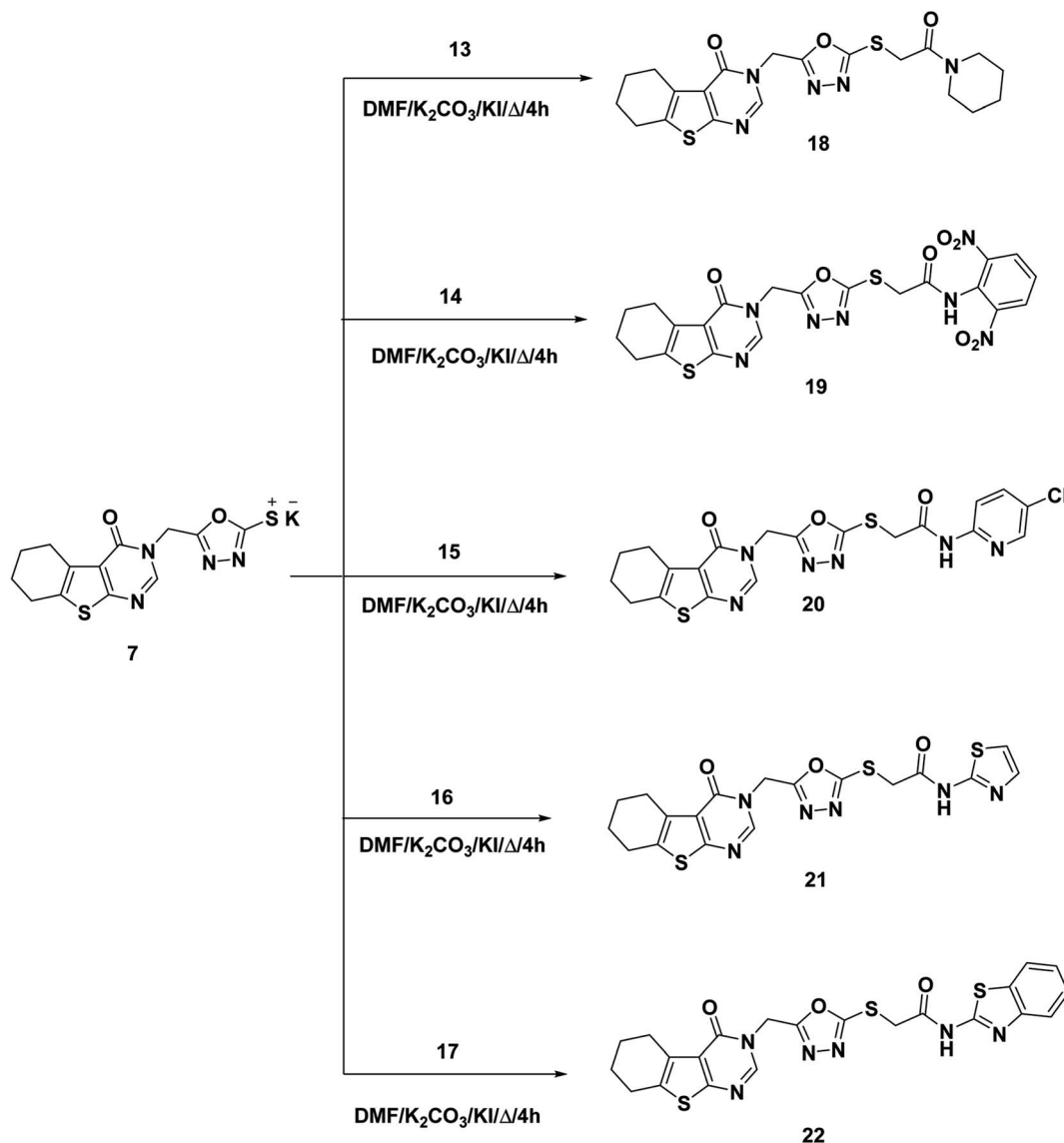
Scheme 3 Synthesis of the target compounds **18–22**.

for drug development and treatment planning. Flow cytometry plays a significant role in detecting apoptotic cells, which are involved in a programmed cell death process. Accurately identifying apoptotic cells is critical for comprehending the

mechanisms of action of anticancer drugs and other treatments. Flow cytometry is an effective method for detecting apoptotic cells and provides important insights into the mechanisms of action of the drug.[44]

2.2.3.1. Cell cycle analysis. In this test, MCF-7 cells were treated with compound **18** (at a concentration of 10.17 μM) for 72 h. Later, the cells were stained with propidium iodide, and their distribution throughout the various cell cycle phases was determined by using a flow cytometric analysis

Table 1 *In vitro* cytotoxicity and VEGFR-2 inhibitory of the obtained thieno[2,3-*d*]pyrimidine derivatives against HepG2 and MCF-7 cell lines

Comp.	IC$_{50}$[a] (μM)		VEGFR-2 IC$_{50}$[a] (μM)
	MCF-7	HepG2	
18	10.17 ± 1.01	24.27 ± 2.08	0.18 ± 0.004
19	16.50 ± 1.16	31.78 ± 1.15	0.29 ± 0.007
20	5.38 ± 0.45	4.84 ± 0.38	0.83 ± 0.017
21	6.31 ± 0.16	11.83 ± 1.05	0.42 ± 0.008
22	5.73 ± 0.18	5.51 ± 0.25	0.26 ± 0.006
Sorafenib	9.98 ± 0.6	13.26 ± 0.3	0.12 ± 0.002

[a] The results are the mean of three experiments.

Table 2 Cell cycle analysis in MCF-7 cells before and after treatment with compound **18**

Sample	Cell cycle distribution (%)		
	%G0–G1	%S	% G2/M
MCF-7	58.02	30.1	11.88
Compound **18**-treated MCF-7	56.46	28.14	15.4

Paper

Table 3 Effect of compound **18** on stages of the cell death process in MCF-7 cells

Sample	Total	Early apoptosis	Late apoptosis	Necrosis
MCF-7	2.57	0.53	0.19	1.85
Compound **18** treated MCF-7	25.76	15.96	7.39	2.41

Table 4 Effect of compound **18** on levels of BAX, Bcl-2, active caspases-8, and active caspases-9

Sample	Protein expression			
	BAX	Bcl-2	Caspase-8	Caspase-9
Cont. MCF-7	1	1	1	1
Compound-**18** treated MCF-7	3.669	0.315	2.607	5.422

Table 5 The effect of compounds **18** on the levels of TNF-α and IL6

Sample	TNF-α	IL6
Cont. MCF-7	1	1
Compound-**18** treated MCF-7	0.335	0.393

technique. The results in Table 2 and ESI Data† demonstrated a decrease in the proportion of MCF-7 cells treated with compound **18** at the G0–G1 and S phases. In the G0–G1 phase, it decreased from 58.02% to 56.46%, and at the S phase, it decreased from 30.1% to 28.14%. The proportion of MCF-7 cells, on the other hand, increased in the compound **18**-treated cells during the G2/M phase (15.4% vs. 11.88% control cells). These findings supported that compound **18** could halt cell growth at the G2/M phase.

2.2.3.2. Apoptosis assay. This method involved staining MCF-7 cells with annexin V and propidium iodide (PI) and then incubating them with compound **18** (at a concentration of 10.17 μM) for 72 h. When compared to untreated control cells, compound **18** caused more MCF-7 cells to undergo apoptosis (Table 3 and ESI Data†). Apoptosis was specifically induced by compound **18** by 23.35% (early apoptosis: 15.96% and late apoptosis: 7.39%), as opposed to 0.72% in control cells (early apoptosis: 0.53% and late apoptosis: 0.19%).

2.2.4. Effects on Bcl-2 family proteins and caspases. The Bcl-2 family plays a significant role in the suppression of the intrinsic apoptotic pathway. The anti-apoptotic Bcl-2 protein stops apoptosis, whereas the pro-apoptotic BAX protein boosts it. Thus, the balance between these two dissimilar and antagonistic proteins controls the fate of the cell.[45] Moreover, caspases are essential for the launch and completion of apoptosis. Caspase-9 and caspase 8 serve as promoters for other lethal caspases. Their activation initiate the caspase cascade to destruct other cellular targets.[46]

In this experiment, the effects of compound **18** at a concentration of 10.17 μM (IC$_{50}$ value) on the BAX, Bcl-2, caspase-8, and caspase-9 in MCF-7 cells were investigated. According to the findings in Table 4, compound **18** elevated BAX levels, a protein that promotes apoptosis, by 3.6-fold and

Table 6 The docking scores of the thieno[2,3-*d*]pyrimidine derivatives and sorafenib against VEGFR-2

Comp.	ΔG [kcal mol^{-1}]
18	−22.71
19	−22.52
20	−21.00
21	−19.99
22	−20.60
Sorafenib	−21.77
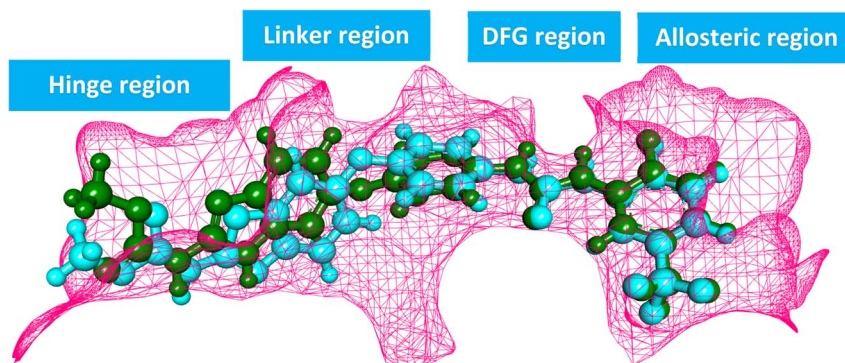
Fig. 3 Superimposition of the native and docked co-crystallized ligand in the active site of VEGFR-2 during the validation of the molecular docking procedure.
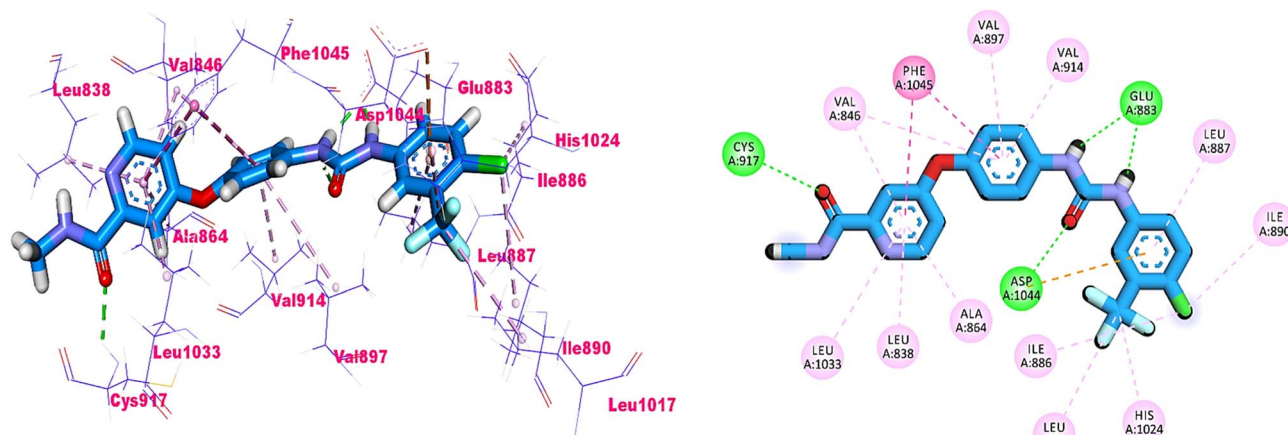
Fig. 4 3D and 2D illustrations of sorafeib in the active site of VEGFR-2.

significantly decreased Bcl-2 levels by 3.1-fold when compared to control cells. As well, compound **18** revealed 2.6-fold higher levels in caspase-8 compared to the control. Additionally, it achieved a significant increase in caspase-9 levels (5.4-fold) in comparison to the control group.

2.2.5.   TNF-α and IL-6 inhibition. Proangiogenic cytokines like TNF-α and IL6 promote angiogenesis and tumor growth. As a result, the ability of compound **18** (the most promising candidate) to reduce TNF-α and IL6 production in MCF-7 cells was examined. TNF-α and IL6 in MCF-7 cells were dramatically lowered by compound **18**, in line with the data shown in Table 5. When compared to control MCF-7 cells, TNF-α and IL6 levels were lower by 2.9 and 2.5 times, respectively.

2.3.   Computational studies

2.3.1.   Molecular docking. Using MOE2019, a molecular docking study was done to determine how precisely the designed candidates **18–22** bind to the VEGFR-2 binding site when compared to the reference drug sorafenib. For performing docking validation, the native co-crystallized inhibitor of VEGFR-2 (PDB ID: 2OH4) was redocked into its binding site. A very low RMSD value (0.88 °A) was produced when the docked pose was lay over the native one, indicating that the validation and hence the docking method was in the positive way (Fig. 3).

The binding energies of the synthesized thieno[2,3-*d*] pyrimidine derivatives were presented in Table 6. Interestingly, the docking results were harmonious with the biological findings where compound **18** (the most promising VEGFR-2 inhibitor) achieved binding score of −22.71 kcal mol⁻¹ against the VEGFR-2 enzyme. This value were higher than other derivatives and sorafenib (−21.77 kcal mol⁻¹).

As shown in Fig. 4, sorafenib's docking pose involved three crucial H-bonding interactions with Cys917, Glu883, and Asp1044. It also engaged in a number of hydrophobic interactions with the hydrophobic pocket created by Leu887, Leu1017, and Ile890.

Compounds **18–22** were able to recognize the VEGFR-2 kinase binding site and interact with important amino acids. The thieno[2,3-*d*]pyrimidine moieties were oriented towards the hinge region and formed several hydrophobic interactions in addition to one H-bond with the Cys917 residue. The 1,3,4-oxadiazole moieties were then incorporated into the linker region and formed hydrophobic interactions with the Val914, Val846, Ala864, Phe1045, and Cys1044. Also, the same compounds interacted *via* two H-bonds with the NH moiety of Asp1044 and the carboxylate side chain of Glu883 of the conserved DFG motif region. Finally, the terminal heads of compounds **18–22** represented by piperidine (**18**), 2,6-dinitrophenyl (**19**), 5-chloropyridine (**20**), thiazole (**21**), and benzo[*d*]thiazole (**22**) interacted Leu887, Ile886, and Ile890 residues and tightly fit the hydrophobic region (Fig. 5). These findings may gave an explanation for the designed candidates' potent VEGFR-2 inhibitory activities.

2.3.2.   Molecular dynamics (MD) simulations. Compound **18** maintained a relatively constant conformation inside the binding pocket and a constant distance from the center of mass of the protein throughout the simulation, as shown by analyses of the production run. In the left subfigure of Fig. 6A, the blue and red lines represent the RMSD value for apo and holo proteins with an average of 2.7 Å and 3 Å, respectively. The right figure shows the histogram of the RMSD values of both systems. As can be seen the distribution of apo VEGFR-2 system shows a nearly normal distribution. On the other hand, the holo VEGFR-2_**18** shows two peaks. The first one is around 3 Å and the second one is around 4.2 Å. The RMSD for compound **18** (Fig. 6B) is also rather steady, fluctuating within an average of 2.4 Å. Fig. 6C showed that the average RoG for both the apo and holo systems is consistently around 20.7 Å and 20.5 Å, respectively. Fig. 6D showed that the average SASA for the apo and holo proteins is 17 656 Å² and 17 378 Å², respectively. Fig. 6E revealed that the overall number of H-bonds is dynamic, with both systems exhibiting fluctuations around 70 bonds. Based on the previous results,

Fig. 5   Binding modes of the synthesized compounds against the active site of VEGFR-2. (A) Compound **18**, (B) compound **19**, (C) compound **20**, (D) compound **21**, (E) compound **22**.

the protein's structure is likely to be stable. The fluctuation of amino acids is quite stable (show fluctuation values of less than 2 Å) in the RMSF plot (Fig. 6F), except for the N-terminus

(10.5 Å for the holo protein), the Arg840:Phe843 loop of the holo protein (2.9 Å), the Tyr994:Asp996 loop of the holo protein (2.3 Å), the Tyr994:Phe997 loop of the apo protein (2.5
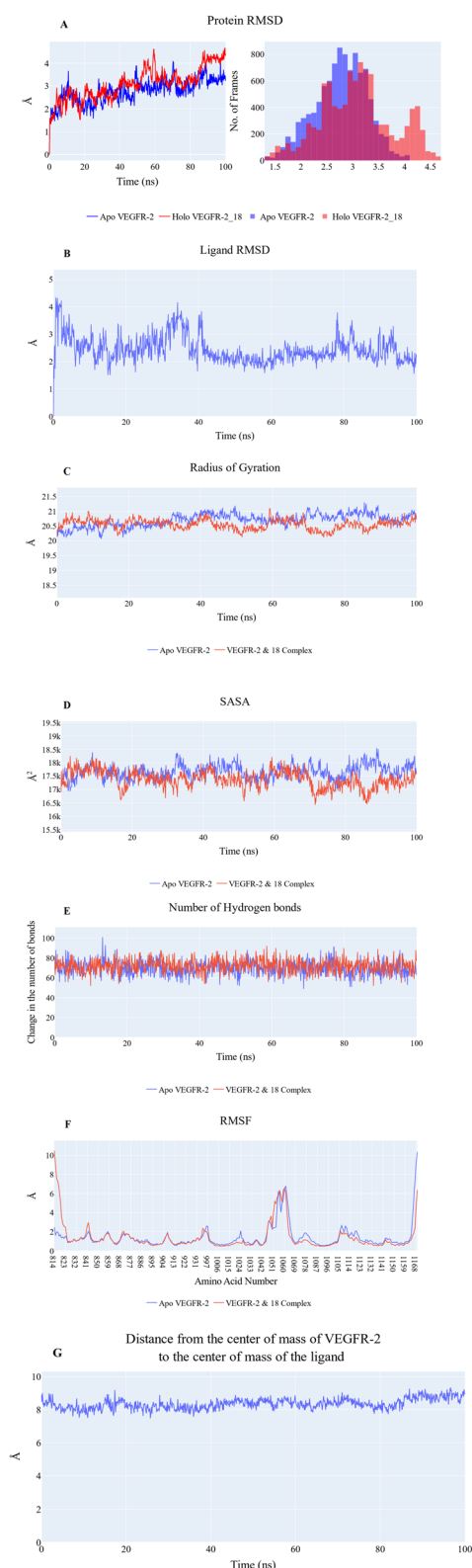
Fig. 6 (A) RMSD values from the trajectory for the VEGFR-2 protein in apo (blue line) and holo forms (red line), (B) the ligand RMSD values, (C) radius of gyration for the VEGFR-2 protein in apo (blue line) and holo forms (red line), (D) SASA for the VEGFR-2 protein in apo (blue line) and holo forms (red line), (E) change in the number of hydrogen bonds for the VEGFR-2 protein in apo (blue line) and holo forms (red line), (F) RMSF for the VEGFR-2 protein in apo (blue line) and holo forms (red

Å), the Gly1046:Leu1065 loop of both systems (6.8 Å), the Pro1106:Ile1112 loop of the apo protein (2.6 Å), and the C terminal (10.3 Å for the apo protein and 6.3 Å for the holo protein). Stable binding occurs between **18** and the VEGFR-2 protein, with an average distance of 8.3 Å between the two centers of masses (Fig. 6G).

2.3.3. MM-GBSA analysis. In Fig. 7, we can see the individual components that make up the binding free energy as calculated using MM-GBSA. Compound **18** showed a binding energy of −40.35 kcal mol^{-1}. The electrostatic contacts contribute moderately to the binding stability since their energy is approximately half that of the hydrophobic interactions (−54.13 kcal mol^{-1} on average for van der Waals interactions and −27.16 kcal mol^{-1} for electrostatic interactions). Using free energy decomposition, we were able to quantify the relative contribution of the amino acids located within 1 nm of **18** (Fig. 8). Leu838 (−1.66 kcal mol^{-1}), Val846 (−1.5 kcal mol^{-1}), Lys866 (−2.04 kcal mol^{-1}), Leu887 (−1.18 kcal mol^{-1}), Val896 (−1.09 kcal mol^{-1}), Val897 (−1.37 kcal mol^{-1}), Val914 (−1.29 kcal mol^{-1}), Leu1033 (−1.18 kcal mol^{-1}), Cys1043 (−4.23 kcal mol^{-1}), Asp1044 (−1.69 kcal mol^{-1}), and Phe1045 (−1.6 kcal mol^{-1}) are the amino acids that have a contribution less than −1 kcal mol^{-1}. Furthermore, Glu883 and Glu915 have a positive binding energy contribution of +0.6 kcal mol^{-1}.

Fig. 9A–C indicated that ten amino acids (Leu838, Val846, Leu887, Leu897, Val914, Leu1017, Leu1033, Cys1043, Asp1044, and Phe1045) exhibit extraordinarily persistent hydrophobic interactions (with at least 93.7% incidence). Asp1044 also has a very high H-bond formation efficiency (94.5%). After obtaining representative frames from the trajectory clustering using TTClust, we utilized PLIP to identify contacts and retrieve 3D binding conformations as.pse files (Fig. 10).

PCA was employed to unveil coordinated motion of high amplitude in the trajectory. Using the scree plot (the eigenvalues *vs.* the eigenvector index) and doing cumulative sums of eigenvalues for each new eigenvector, allowed us to calculate the number of eigenvectors that would represent the essential subspace (Fig. 11). In this case, as can be seen, the first three eigenvectors accounted for almost 87% of the overall variance, with the first eigenvector alone accounting for 75%. Furthermore, the distribution of eigenvectors values of the first PCs is often non-Gaussian. The first two eigenvectors have separated peaks, whereas the third and fourth PCs have peaks that are not totally separated and the remainder starts to show a Gaussian distribution (Fig. 12). The VEGFR-2 cosine content was determined in both the apo and holo simulations to establish the randomness of the motion captured by the first 10 eigenvectors. From what can be seen in Fig. 13, all of the first ten PCs, except for the second one (0.5), in the holo simulation have cosine content values below 0.2, indicating that they are not a random motion. The results of the apo simulation, except for the third eigenvector

line), (G) distance from the center of mass of compound **18** and VEGFR-2 protein.
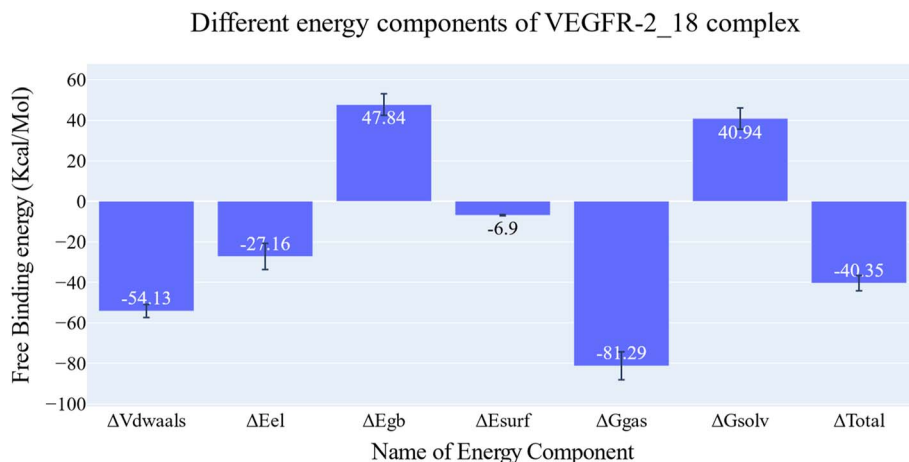
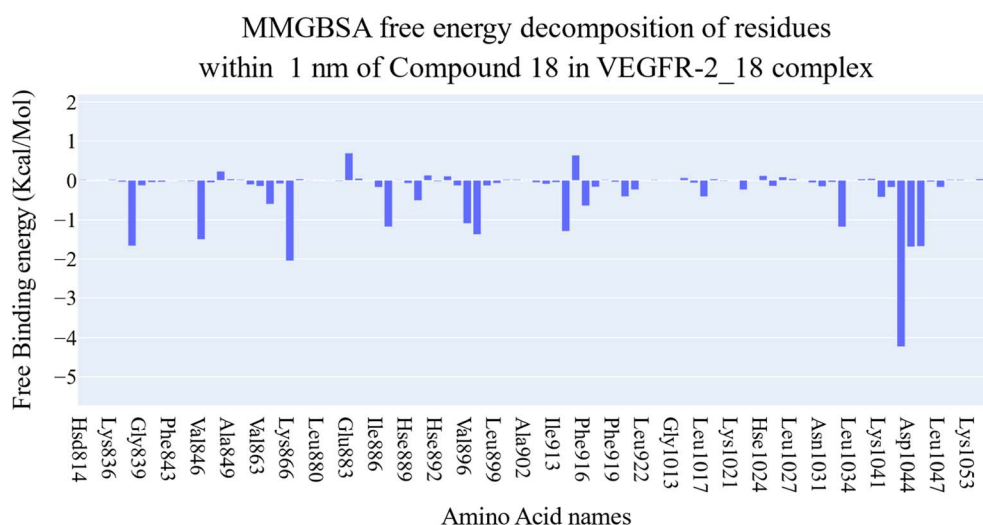**Fig. 7** Different energetic components of MM-GBSA and their values. Bars represent the standard deviations.

Fig. 8 Binding free energy decomposition of the VEGFR-2_**18** complex.

(cosine content of 0.22), follow the same pattern. Thus, the first three eigenvectors were selected to reflect the essential subspace. The root mean square inner product (RMSIP) shows that there is only a 27.8% overlap between the two subspaces (the first three eigenvectors), indicating that the two trajectories were sampled differently. We also determined the overlap between the apo and holo trajectory C matrices and it was 37% similar.

As a way to evaluate how similarly sampled the two trajectories are, we projected each trajectory onto the first three eigenvectors of the combined C matrix (Fig. 14–16). In these diagrams, the average structure of each trajectory was shown as a bigger marker, and the projections were made using the first three main components in combinations of two. Fig. 14 (projection on the first two eigenvectors) revealed a sparse overlap between the two trajectories and a wide gap

between the two average structures. Fig. 15 demonstrated that the average structures of the two trajectories are quite similar and that there is a lot of overlap between the two trajectories when projected on the first and third eigenvectors. Lastly, a projection on the second and third eigenvectors (Fig. 16) revealed a moderate overlap between the two trajectories and a separation between the average structures similar to that of Fig. 14. Porcupine figures were also made to illustrate the motion captured in the first three eigenvectors in the two simulations (Fig. 17). These three eigenvectors all capture motion from the Gly1046:Leu1065 loop opening, but in different directions.

2.3.4. DFT. Computational chemistry is used in the development of novel drugs and materials to solve numerical problems. Currently, a range of computer technologies has been used to analyze the structure and physical properties of
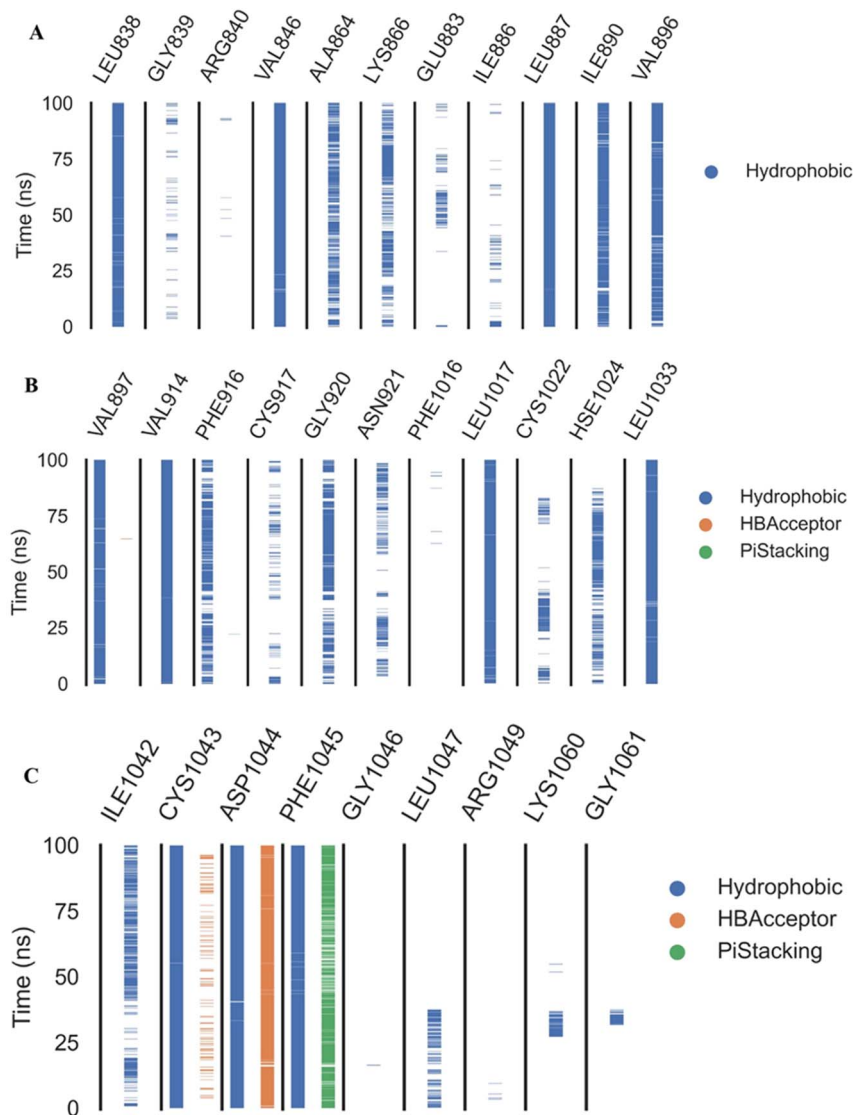
Fig. 9 The amino acids, the types of interactions with compound **18**, and their occurrence during the whole simulation time using the ProLIF python library. (A) Amino acid sequence from LEU838 to VAL896, (B) amino acid sequence from VAL896 to LEU1033, and (C) amino acid sequence from ILE1042 to GLY1061.
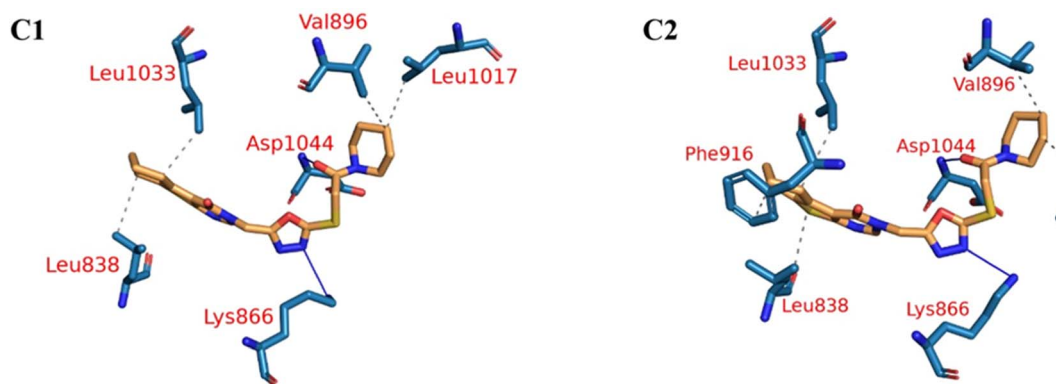

Fig. 10 The two clusters representative obtained from TTClust and their 3D interactions with the molecule **18**. Grey dashed lines: hydrophobic interactions, blue solid lines: H-bonds, orange sticks: molecule **18**, blue sticks: amino acids of VEGFR-2 protein.
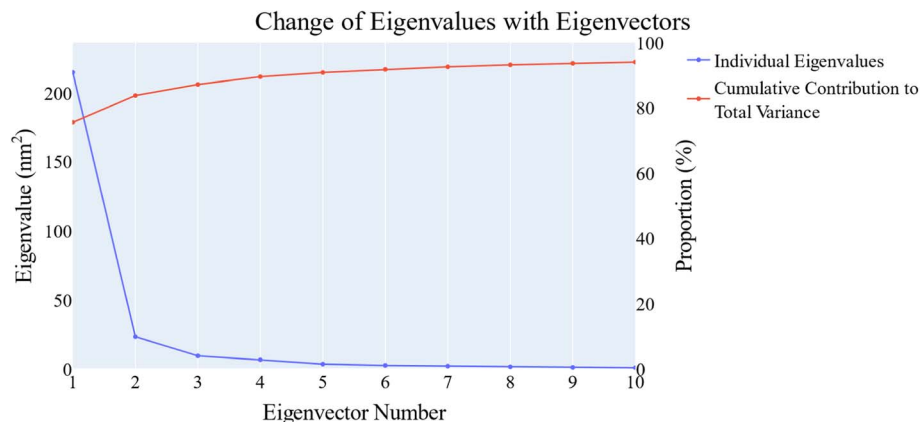
Fig. 11 The change in the eigenvalues with increasing the eigenvectors (blue line). In addition, the cumulative variance retained in the eigenvectors is shown (red line).
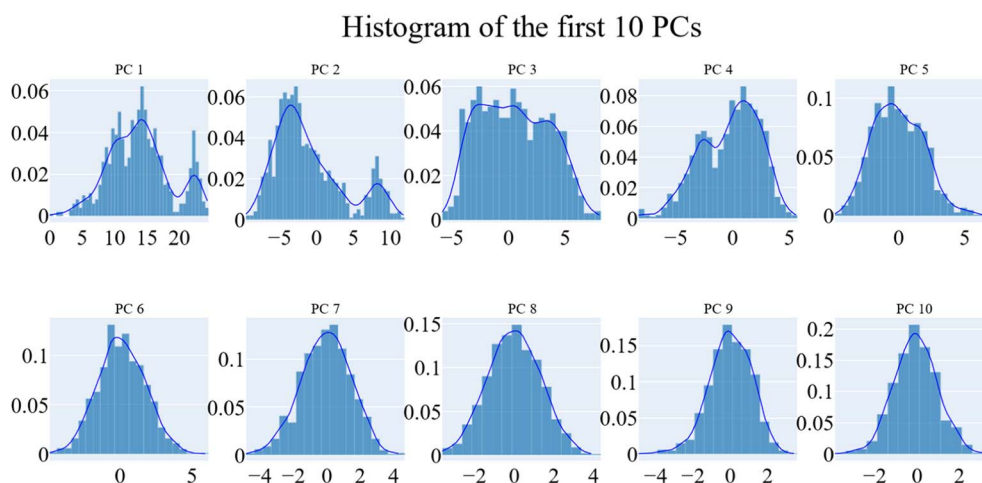

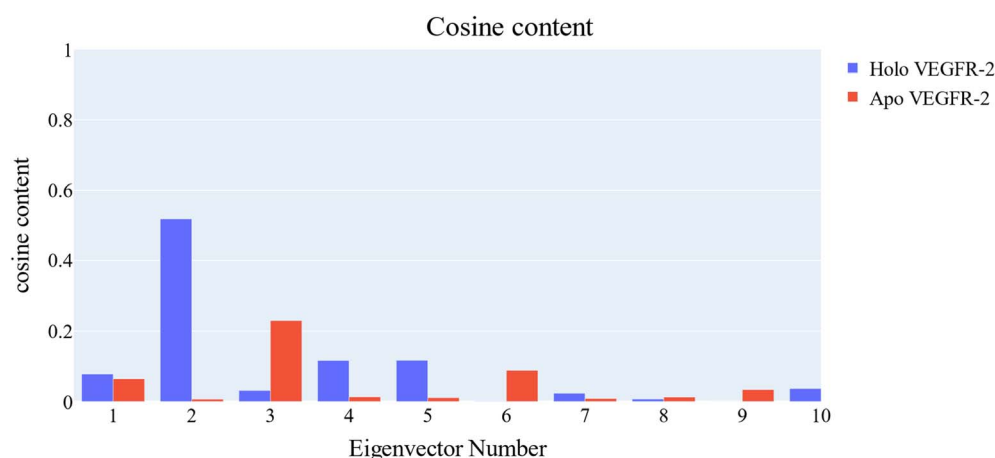**Fig. 12** The distribution of the first ten eigenvectors.

Fig. 13 Values of the cosine content of the first ten eigenvectors for the two trajectories.

medicinal substances. Density functional theory (DFT) is a well-liked technique for characterizing the structural and electrical properties of bioactive molecules. DFT uses the B3LYP functional and 6-311++G (d,p) basis set to look at and simulate various molecular aspects, such as optical, spectral, and charge density. The optimized structure of **18** in Fig. 18a
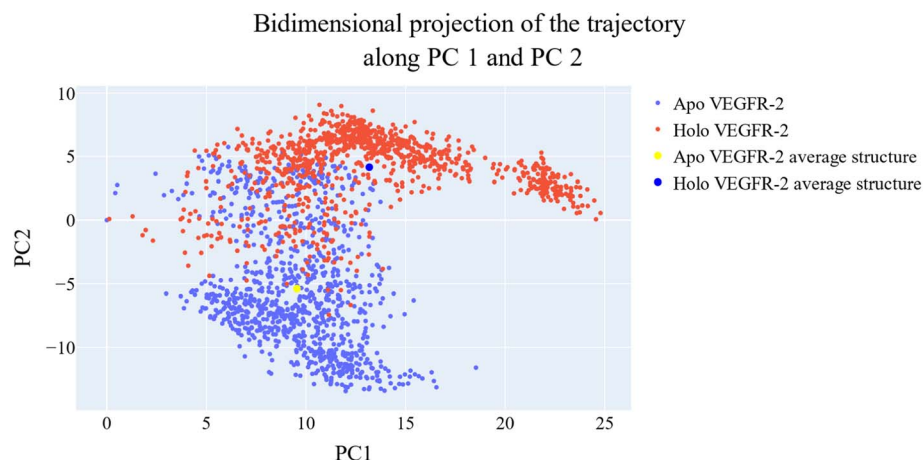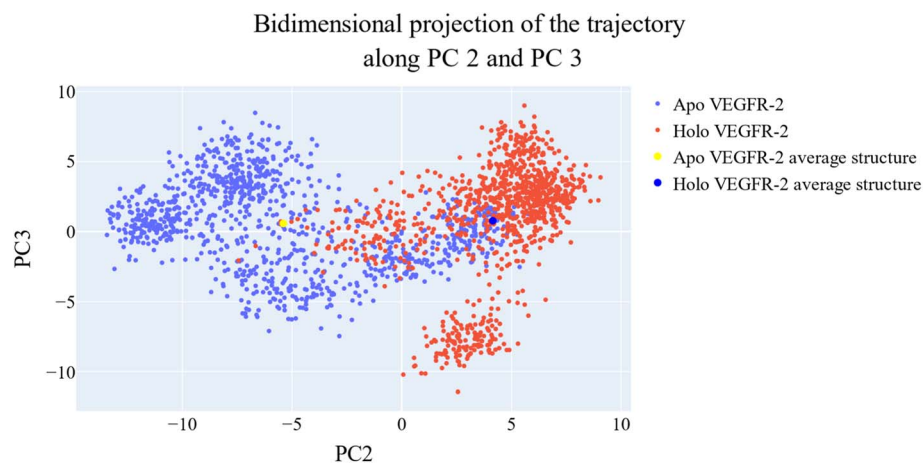
Fig. 14 The projection of each trajectory on the first two eigenvectors. Small blue dots are the frames of the VEGFR-2 in the apo simulation, red blue dots are the frames of the VEGFR-2 in the holo simulation, the large yellow dot is the average structure of VEGFR-2 from the apo simulation, and the large blue dot is the average structure of VEGFR-2 from the holo simulation.
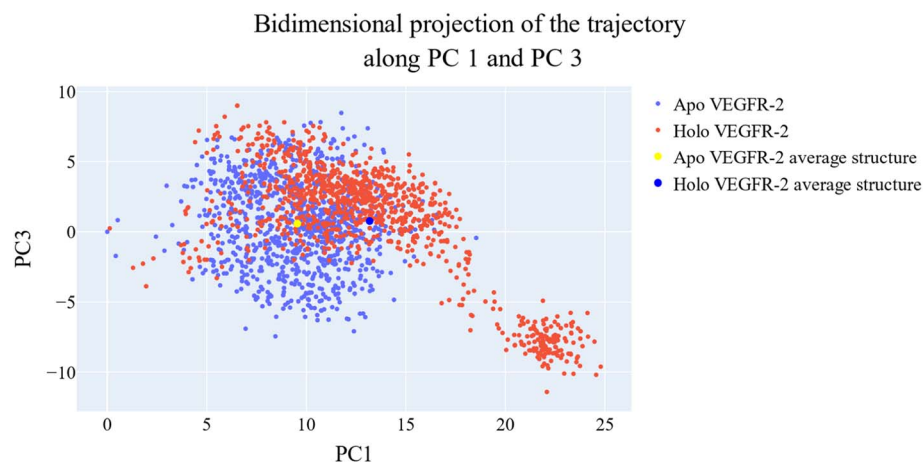
Fig. 15 Shows the projection of each trajectory on the first and third eigenvectors. Small blue dots are the frames of the VEGFR-2 in the apo simulation, red blue dots are the frames of the VEGFR-2 in the holo simulation, the large yellow dot is the average structure of VEGFR-2 from the apo simulation, the large blue dot is the average structure of VEGFR-2 from the holo simulation.

Fig. 16 The projection of each trajectory on the second and third eigenvectors. Small blue dots are the frames of the VEGFR-2 in the apo simulation, red blue dots are the frames of the VEGFR-2 in the holo simulation, the large yellow dot is the average structure of VEGFR-2 from the apo simulation, and the large blue dot is the average structure of VEGFR-2 from the holo simulation.
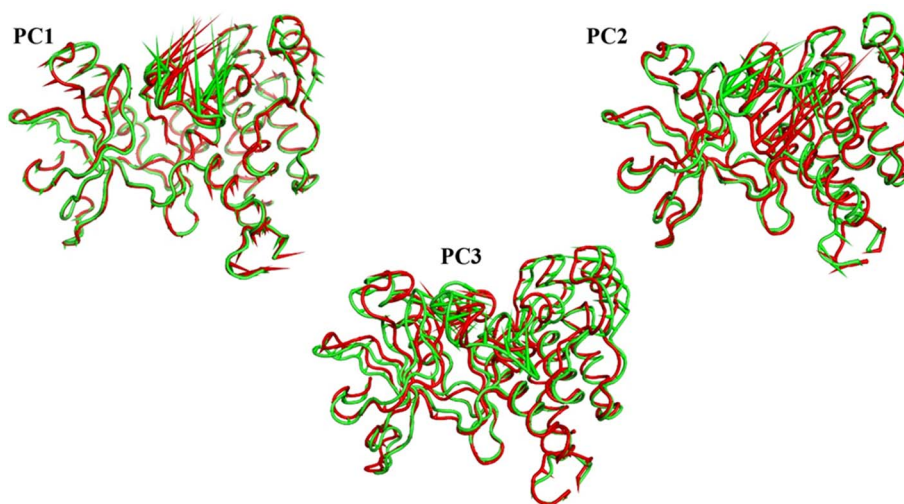
Fig. 17 The porcupine figures of each of the first three eigenvectors for both systems. Green cartoon: apo protein trajectory, red cartoon: holo protein trajectory.

revealed that the doublet state molecule has 55 atoms and 241 electrons, and the predicted dipole moment, D_m, is 7.77 Debye. The D_m value denotes effective charge transfer, high reactivity, and substantial internal interaction. Mulliken charge analysis results showing high charge separation inside the chemical system provide confirmation of high reactivity. The findings of the Mulliken charge distribution in Fig. 18b demonstrate that all oxygen, sulfur, and nitrogen atoms (except for N12) have negative charges. The C15 and C6 atoms gain the most negative charge of all the carbon atoms, as seen in Fig. 18b. Since C16 and C9 have the largest positive charge of all the carbon atoms in compound **18**, they are targets of nucleophilic assault on the molecule, while C15 and C6 are targets of electrophilic attack.

The energy of both HOMO and LUMO is estimated in order to broaden the theoretical calculations, and their density distributions are examined and shown in Fig. 18c. The predicted energies of HOMO and LUMO are found to be −4.605 eV and −1.834 eV, respectively, whereas the energy gap between HOMO and LUMO, or E_{gap}, is found to be 2.77 eV which is relatively small. A reasonable E_{gap} value like this shows that the **18** may be bioactive [**https://www.sciencedirect.com/science/article/abs/pii/S1476927123001196?via%3Dihub**]. The frontier molecular energy gap, E_{gap}, controls the chemical reactivity and stability of the molecule. Ionization ability and electron affinity are both intimately correlated with the HOMO and LUMO energies, respectively. The global reactivity parameters, electron affinity, and ionization potential were theoretically computed using Koopmans' theorem (as detailed in the ESI Data file†) and are shown in Table 7. The electron affinity can be used in combination with ionization energy to give electronic chemical potential, μ, softness (σ) and hardness (η). The value of global softness and hardness suggests that compound **8** is soft and could show potent

biological reactivity.[47] The findings demonstrated the kinetic stability and potential bioactivity of compound **18**.[48]

In order to shed light on the theoretical computation of compound **18** structure, the electrostatic potential, or ESP, is examined. Fig. 18d showed the ESP map of the titled compound. The ESP colored map determines compound **18** chemical reactivity sites and how they will respond to the target. According to the results, huge negative ESP zones are centered around oxygen and nitrogen atoms (red zones) on a scale from 7.04×10^{-2} to -7.04×10^{-2}, whereas big positive ESP zones are found over hydrogen atoms in the blue zones. The residue of the molecule appears to be almost neutral and is prepared for attacks from hydrophobic centers. Although the positive active sites are hydrogen bond donors, the negative ESP sites are hydrogen bond acceptors. The investigation therefore shows that the bioactive compound may interact with the target in a successful manner.[49]

Gauss Sum analysis of the overall density of states was shown in Fig. 18e. The compound **18** spectra demonstrated the alpha and beta density of states (DOS) as well as the total density of states (TDOS). The filled orbitals under HOMO have the largest electronic density.

Quantum Theory of Atoms in Molecules (QTAIM) offers a formal method for breaking down molecule attributes into atomic components based on the topological electron density; (ρ) using the assistance of AIMALL and Multiwfn programs. This procedure clarifies the theoretical calculations and interactions within the compound **18** molecule. The overall energy density, $H(r)$, and the Laplacian values, ($\nabla^2\rho$), of the newly established bond critical points (BCPs), were used as local variables to evaluate the covalent or ionic nature of chemical interatomic interactions within compound **18**. Large (ρ), low (negative) $\nabla^2\rho$ and positive $H(r)$ values at the BCPs were expected for bonds with a high increment of covalent character. Fig. 18f and g, respectively, showed the
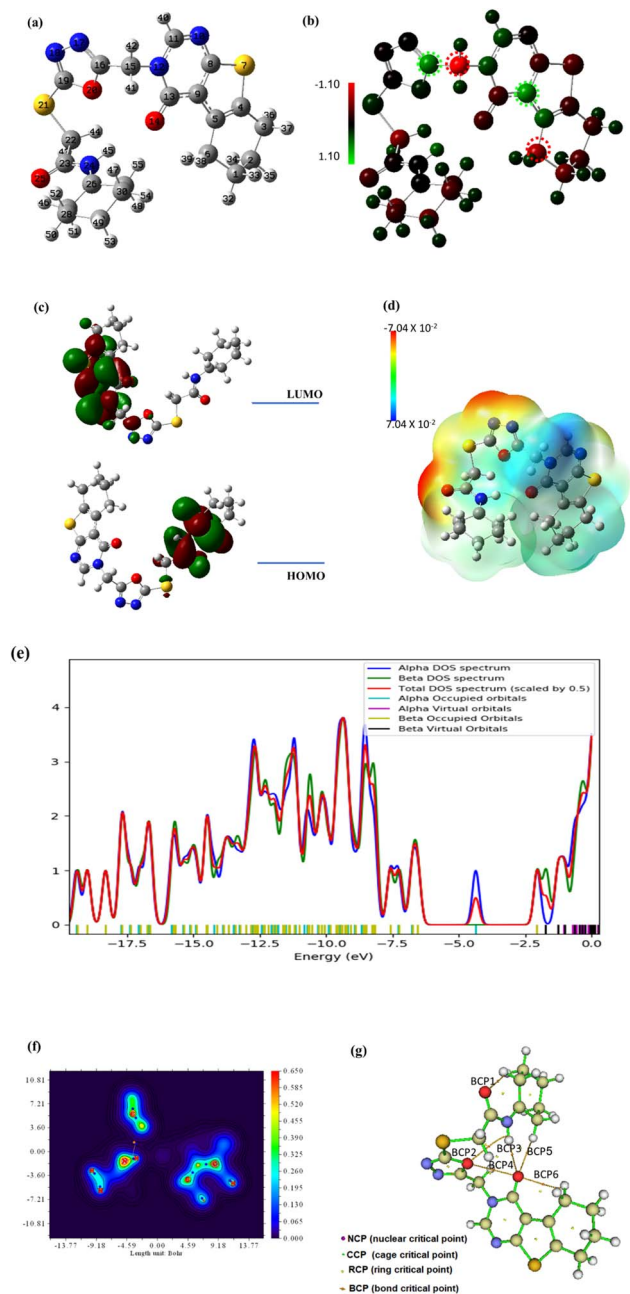
Fig. 18 The optimized geometry (a), the Mullikan atomic charge distribution (b), the frontier molecular orbitals (c), the electrostatic potential (d), the total density of states (e), and the QTAIM maps (f and g) at B3LYB/6-311+G(d,p) for compound **18**.

QTAIM molecular map and filled contour map, while ESI Data† provide the full QTAIM BCPs and routes. The QTAIM parameters in ESI Data† validated the prepared molecule's

stability because the most significant BCPs (six BCPs) were produced with (ρ) less than 0.1 and positive ($\nabla^2 \rho$) values, which indicated noncovalent or closed bonding. Moreover, the calculated $H(r)$ confirms that the created BCPs are electrostatic, which contributes to the stability of compound **18**.

2.3.5. *In silico* ADME analysis. Poor pharmacokinetics and toxicity are frequently cited as significant causes of costly late-stage drug development failures.[50] Thus, there is a growing recognition that these factors should be addressed as early as possible in the drug discovery process.[51] Computational techniques are used to predict properties related to absorption, distribution, metabolism, excretion (ADME), and toxicity, in order to identify compounds that may lead to late-stage failures before large-scale production.[52] Quantitative structure–activity relationship (QSAR) methods are commonly employed in computational ADMET studies, which use statistical approaches to establish correlations between a given property and a set of molecular and structural descriptors of the compounds being evaluated.[53] Thieno[2,3-*d*] pyrimidine derivatives were evaluated for their ADME characteristics using computational methods with sorafenib serving as a reference molecule. The computational analysis, presented in Fig. 19 and Table 8 and performed using Discovery Studio 4.0, indicated that all compounds had limited ability to penetrate the blood–brain barrier (L-BBB). However, most of the compounds displayed favourable levels of aqueous solubility (L-Sol) and intestinal absorption (L-Abs). The compounds were also predicted to be non-hepatotoxic (Hep-T), free of any inhibitory effects on cytochrome P4502D6, and exhibited plasma protein.

2.3.6. Toxicity studies. The synthesized thieno[2,3-*d*] pyrimidine derivatives were evaluated for their toxicity characteristics using computational methods with sorafenib serving as a reference molecule. Using the Discovery Studio software,[54,55] analysis was based on the findings from the seven toxicity models presented in Table 9. Notably, all of the synthesized members were non toxic against DTP model. Also, with the exception of compound **21**, all members displayed no mutagenicity as predicted by the Ames test. When compared to sorafenib (14.244 mg kg^{-1} day^{-1}), the computed carcinogenic potency TD$_{50}$ values of the tested compounds ranged from 5.036 to 30.514 mg kg^{-1} day^{-1}. Furthermore, the predicted oral LD$_{50}$ values of the synthesized members exceeded that of sorafenib (0.823 g kg^{-1}), ranging from 2.950 to 6.240 g kg^{-1}. Additionally, the calculated LOAEL values for the synthesized compounds, which varied from 0.043 to 0.114 g kg^{-1}, surpassed those of sorafenib (0.005 g kg^{-1}). Finally, it was predicted that the synthetic compounds would only mildly irritate the eyes in the ocular irritancy model.

Table 7 The DFT calculated global reactivity parameters for compound **18**

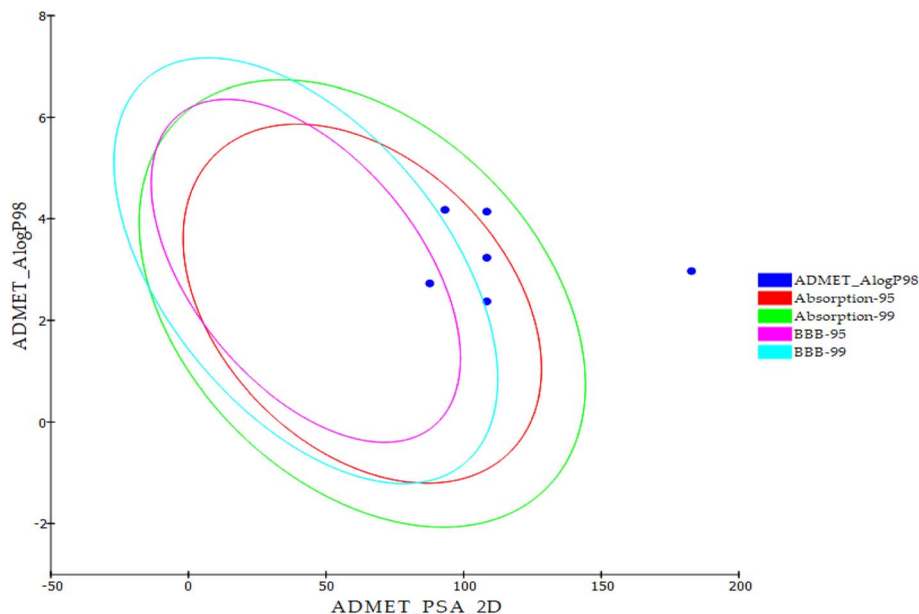| IP	EA	μ (eV)	χ (eV)	η (eV)	σ (eV)	ω (eV)	Dm (Debye)	TE (eV)	ΔN_{max}	ΔE (eV)
4.605	1.834	−3.219	3.219	1.386	0.722	7.181	7.772	−57439.9	2.323	−7.181

Fig. 19 *In silico* ADME output.

Table 8 ADMET screening of the synthesized compounds

Code	Comp.	BBB level	Solubility level	Absorption level	CYP2D6 prediction	PPB prediction
18	18	Low	Low	Good	No inhibition	<90%
19	19	Very low		Very poor		
20	20			Good		>90%
21	21					<90%
22	22			Moderate		>90%
Sorafenib			Very low	Good		

Table 9 Toxicity study of the synthesized compounds

Code	Ames prediction	DTP	Carcinogenic potency TD$_{50}$ (rat)[a]	Rat maximum tolerated dose (feed)[b]	Rat oral LD$_{50}$[b]	Rat chronic LOAEL[b]	Ocular irritancy
18	Non-mutagen	Non-	12.453	0.016	2.950	0.070	Mild
19	Mutagen	toxic	30.514	0.019	3.244	0.094	
20	Non-mutagen		5.036	0.044	3.652	0.043	
21	Mutagen		8.295	0.024	5.760	0.088	
22	Non-mutagen		6.388	0.026	6.240	0.114	
Sorafenib		Toxic	14.244	0.089	0.823	0.005	

[a] Unit: mg per kg body weight per day. [b] Unit: g per kg body weight.

3. Conclusion

In conclusion, this study demonstrates the potential of thieno[2,3-*d*]pyrimidine derivatives as potent and selective anti-cancer agents that target VEGFR-2. Compound **18**, in particular, was found to have strong anti-VEGFR-2 activity and to effectively inhibit cancer cell growth *in vitro* in both MCF-7 and HepG2 cancer cell lines. Further investigation showed that compound **18** induced cell cycle arrest at G2/M phase and

apoptosis in MCF-7 cancer cells, and was able to modulate the expression of key apoptotic genes such as BAX and Bcl-2, as well as caspase-8 and caspase-9. In addition, computational techniques such as molecular docking, MD simulations, and PLIP provided valuable insights into the structural and energetic features of the VEGFR-2-**18** complex, further supporting the potential of this compound as a promising anti-cancer agent. The use of DFT calculations also provided insights into the geometry and electronic properties of

compound **18**. Finally, computational ADMET studies suggest that these thieno[2,3-*d*]pyrimidine derivatives have good drug development potential. Overall, the study provides a foundation for further research, highlighting the potential of thieno [2,3-*d*]pyrimidine derivatives as a new class of anticancer agents, and offering guidance for future drug discovery efforts.

4. Experimental

4.1. Chemistry

4.1.1. General. All apparatus and fine chemicals used in the synthesis of the target compound were clarified in ESI Data.† The reported compounds **1**,[37] **2**,[38] **4**,[39] **5**,[40] **6**,[40] and **13–17** (ref. 56 and 57) were synthesized according to the reported procedure.

4.1.2. Synthesis of the target compounds 18–22. A mixture of the potassium salt of 3-((5-mercapto-1,3,4-oxadiazol-2-yl) methyl)-5,6,7,8-tetrahydrobenzo[4,5]thieno[2,3-*d*]pyrimidin-4(3*H*)-one **7** (0.02 mol) and the appropriate 2-chloro-*N*-substitutedacetamide derivatives **13–17** (0.02 mol) and KI (0.001 mol) in DMF (10 ml) was refluxed on a water bath for 4 h. The reaction mixtures were poured on crushed ice. The precipitates were collected and crystalized from ethanol to give the corresponding target compounds **18–22**.

4.1.2.1. 3-((5-((2-Oxo-2-(piperidin-1-yl)ethyl)thio)-1,3,4-oxadiazol-2-yl)methyl)-5,6,7,8-tetrahydrobenzo[4,5]thieno[2,3-d]pyrimidin-4(3H)-one 18.
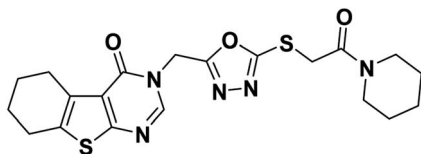
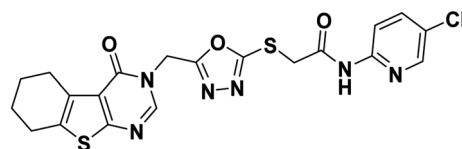White crystal (yield, 75%); m. p. = 204–206 °C; ^{1}H NMR (400 MHz, DMSO-d_6) δ 8.46 (s, 1H, Ar–H pyrimidine), 5.44 (s, 2H, N–CH$_2$), 4.46 (s, 2H, S–CH$_2$), 3.41 (d, 4H, 2CH$_2$ piperidine), 2.86 (m, 2H, CH$_2$), 2.77 (m, 2H, CH$_2$), 1.77 (m, 4H, 2CH$_2$), 1.57 (m, 4H, 2CH$_2$ piperidine), 1.43 (m, 2H, CH$_2$ piperidine); ^{13}C NMR (101 MHz, DMSO-d_6) δ 164.57, 164.41, 163.68, 162.07, 156.92, 147.71, 134.23, 131.36, 122.13, 46.85, 43.07, 37.43, 26.18, 25.71, 25.59, 25.00, 24.18 (2C), 22.80, 22.15; for $C_{20}H_{23}N_5O_3S_2$ (445.56).

4.1.2.2. N-(2,6-Dinitrophenyl)-2-((5-((4-oxo-5,6,7,8-tetrahydrobenzo[4,5]thieno[2,3-d]pyrimidin-3(4H)-yl)methyl)-1,3,4-oxadiazol-2-yl)thio)acetamide 19.
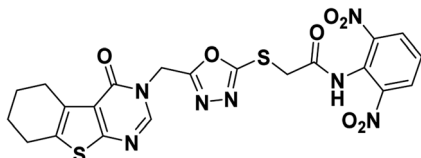

Yellow crystal (yield, 70%); m. p. = 238–240 °C; IR (KBr) ν cm^{-1}: 3291 (NH), 2931 (CH aliphatic), 1661 (C=O); ^{1}H NMR (400 MHz, DMSO-d_6) δ 8.89 (m, 1H, Ar–H), 8.27 (s, 1H, Ar–H pyrimidine) 8.05 (m, 3H, Ar–H), 4.97 (s, 2H, N–CH$_2$), 4.29 (s, 2H, S–CH$_2$), 2.88 (m, 2H, CH$_2$), 2.77 (m, 2H, CH$_2$), 1.78 (s, 4H, 2CH$_2$); for $C_{21}H_{17}N_7O_7S_2$ (543.53).

4.1.2.3. N-(5-Chloropyridin-2-yl)-2-((5-((4-oxo-5,6,7,8-tetrahydrobenzo[4,5]thieno[2,3-d]pyrimidin-3(4H)-yl)methyl)-1,3,4-oxadiazol-2-yl)thio)acetamide 20.


Off-white crystal (yield, 77%); m. p. = 225–227 °C; IR (KBr) ν cm^{-1}: 3291 (NH), 2929 (CH aliphatic), 1666 (C=O); ^{1}H NMR (400 MHz, DMSO-d_6) δ 11.06 (s, 1H, NH), 8.44 (s, 1H, Ar–H pyrimidine), 8.38 (d, J = 2.7 Hz, 1H, Ar–H), 8.02 (d, J = 8.9 Hz, 1H, Ar–H), 7.89 (dd, J = 8.9, 2.7 Hz, 1H, Ar–H), 5.43 (s, 2H, N–CH$_2$), 4.34 (s, 2H, S–CH$_2$), 2.84 (m, 2H, CH$_2$), 2.76 (m, 2H, CH$_2$), 1.77 (m, 4H, 2CH$_2$); ^{13}C NMR (101 MHz, DMSO-d_6) δ 166.21, 164.15, 163.97, 162.05, 156.90, 150.63, 147.64, 146.91, 138.50, 134.17, 131.33, 125.93, 122.08, 114.97, 40.67, 36.97, 25.67, 24.98, 22.78, 22.13; for $C_{20}H_{17}ClN_6O_3S_2$ (488.97).

4.1.2.4. 2-((5-((4-Oxo-5,6,7,8-tetrahydrobenzo[4,5]thieno[2,3-d]pyrimidin-3(4H)-yl)methyl)-1,3,4-oxadiazol-2-yl)thio)-N-(thiazol-2-yl)acetamide 21.
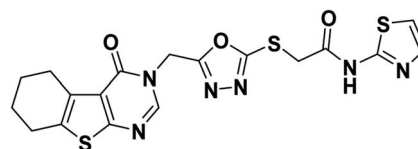
Orange crystal (yield, 80%); m. p. = 230–232 °C; IR (KBr) ν cm^{-1}: 3307 (NH), 2931 (CH aliphatic), 1673 (C=O); ^{1}H NMR (400 MHz, DMSO-d_6) δ 8.45 (s, 1H, Ar–H pyrimidine), 7.46 (d, J = 3.6 Hz, 1H, Ar–H), 7.18 (d, J = 3.6 Hz, 1H, Ar–H), 5.44 (s, 2H, N–CH$_2$), 4.34 (s, 2H, S–CH$_2$), 2.84 (m, 2H, CH$_2$), 2.74 (m, 2H, CH$_2$), 1.76 (m, 4H, 2CH$_2$); ^{13}C NMR (101 MHz, DMSO-d_6) δ 164.23, 164.00, 162.07, 156.92, 147.66, 138.08, 134.17, 131.36, 122.11, 113.98, 113.86, 40.67, 25.69, 25.00, 22.80, 22.15; for $C_{18}H_{16}N_6O_3S_3$ (460.55).

4.1.2.5. N-(Benzo[d]thiazol-2-yl)-2-((5-((4-oxo-5,6,7,8-tetrahydrobenzo[4,5]thieno[2,3-d]pyrimidin-3(4H)-yl)methyl)-1,3,4-oxadiazol-2-yl)thio)acetamide 22.
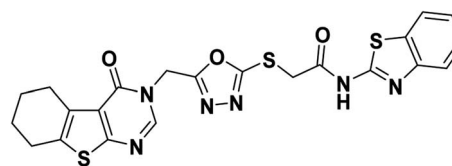
Yellowish white crystal (yield, 78%); m. p. = 224–226 °C; IR (KBr) ν cm^{-1}: 3400 (NH), 2928 (CH aliphatic), 1674 (C=O); ^{1}H NMR (400 MHz, DMSO-d_6) δ 12.74 (s, 1H, NH), 8.44 (s, 1H, Ar–H pyrimidine), 7.97 (d, J = 7.9 Hz, 1H, Ar–H), 7.76 (d, J = 8.0 Hz, 1H, Ar–H), 7.45 (t, J = 7.6 Hz, 1H, Ar–H), 7.32 (t, J = 7.6 Hz, 1H, Ar–H), 5.44 (s, 2H, N–CH$_2$), 4.42 (s, 2H, S–CH$_2$), 2.84 (d, 2H, CH$_2$), 2.72 (m, 2H, CH$_2$), 1.76 (m, 4H, 2CH$_2$); ^{13}C NMR (101 MHz, DMSO-d_6) δ 166.71, 164.08, 163.97, 162.05, 158.26, 156.90, 148.89, 147.61, 134.16, 131.95, 131.31, 126.65, 124.16, 122.20,

122.07, 121.11, 40.66, 36.18, 25.67, 24.93, 22.76, 22.11; for $C_{22}H_{18}N_6O_3S_3$ (510.61).

4.2. Biological examinations

4.2.1. *In vitro* anti-proliferative activity. The synthesized thieno[2,3-*d*]pyrimidine compounds were subjected to an *in vitro* evaluation to appraise their inhibitory potential against the proliferation of MCF-7 and HepG2 cancer cells *via* the implementation of the MTT assay.[58–60] Elaboration on the details of this experimental methodology can be found in the ESI Data section† of the research.

4.2.2. *In vitro* VEGFR-2 inhibition. The synthesized thieno[2,3-*d*]pyrimidine compounds were subjected to an *in vitro* evaluation to appraise their inhibitory potential against VEGFR-2 *via* the implementation of VEGFR-2 ELISA kit.[61] Elaboration on the details of this experimental methodology can be found in the ESI Data section† of the research.

4.2.3. Flow cytometry assay. The potential inhibition of compound **18** on MCF-7 apoptosis and cell cycle analysis was evaluated through the use of flow cytometry. Elaboration on the details of this experimental methodology can be found in the ESI Data section† of the research.

4.2.4. BAX, Bcl-2 and caspases determination. The potential inhibition of compound **18** on BAX, Bcl-2 and caspases level in MCF-7 cells was evaluated through the use of RT-PCR analysis. Elaboration on the details of this experimental methodology can be found in the ESI Data section† of the research.

4.2.5. TNF-α and IL6 a determination. The potential inhibition of compound **18** on the levels of TNF-α and IL6 in cell culture supernatants of MCF-7 was evaluated through the use of ELISA technique. Elaboration on the details of this experimental methodology can be found in the ESI Data section† of the research.

4.3. *In silico* studies

4.3.1. Docking studies. The potential inhibition of the synthesized thieno[2,3-*d*]pyrimidine compounds against VEGFR-2 [PDB ID: 2OH4, resolution: 2.05 Å] was evaluated computationally by docking studies using MOE2019 software. Elaboration on the details of this experimental methodology can be found in the ESI Data section† of the research.[12,62]

4.3.2. MD simulations. The potential inhibition of compound **18** on the VEGFR-2 was evaluated computationally by MD simulation studies were directed by CHARMM-GUI web server[63] and GROMACS 2021 (ref. 64 and 65) as an MD engine. Elaboration on the details of this experimental methodology can be found in the ESI Data section† of the research.

4.3.3. MM-GBSA analysis. MM-GBSA analysis of VEGFR-2-compound **18** complex was evaluated by the Gmx_MMPBSA package.[66,67] Elaboration on the details of this experimental methodology can be found in the ESI Data† section of the research.

4.3.4. ProLIF analysis. ProLIF analysis of VEGFR-2-compound **18** complex was evaluated by GROMACS package.[68–70] Elaboration on the details of this experimental methodology can be found in the ESI Data† section of the research.

4.3.5. Essential dynamics (ED) analysis. Essential Dynamics (ED) analysis of VEGFR-2-compound **18** complex was evaluated by GROMACS by utilizing the gmx covar command.[71] Elaboration on the details of this experimental methodology can be found in the ESI Data section† of the research.

4.3.6. Cosine content analysis. Cosine Content analysis of VEGFR-2- compound **18** complex was evaluated by GROMACS.[72] Elaboration on the details of this experimental methodology can be found in the ESI Data section† of the research.

4.3.7. Bidimensional projections analysis. Bidimensional projections analysis of VEGFR-2-compound **18** complex was evaluated by GROMACS[73,74] elaboration on the details of this experimental methodology can be found in the ESI Data section† of the research.

4.3.8. Density function theory (DFT) calculations. DFT analyses was evaluated for compound **18** by Gaussian software. Elaboration on the details of this experimental methodology can be found in the ESI Data section† of the research.[11]

4.3.9. ADMET studies. ADMET profiles of the synthesized thieno[2,3-*d*]pyrimidine compounds were evaluated computationally by Discovery Studio 4.0. Elaboration on the details of this experimental methodology can be found in the ESI Data section† of the research.[75]

4.3.10. Toxicity studies. The toxicity profiles of the synthesized thieno[2,3-*d*]pyrimidine compounds were evaluated computationally Discovery Studio 4.0. Elaboration on the details of this experimental methodology can be found in the ESI Data section† of the research.[76]

Conflicts of interest

There are no conflicts of interest to declare.

Acknowledgements

References

1 F. Biemar and M. Foti, *Cancer Biol. Med.*, 2013, **10**, 183.
2 R. A. Ward, S. Fawell, N. Floc'h, V. Flemington, D. McKerrecher and P. D. Smith, *Chem. Rev.*, 2020, **121**, 3297–3351.
3 A. Belal, N. M. Abdel Gawad, A. B. Mehany, M. A. Abourehab, H. Elkady, A. A. Al-Karmalawy and A. S. Ismael, *J. Enzyme Inhib. Med. Chem.*, 2022, **37**, 1884–1902.
4 R. Trenker and N. Jura, *Curr. Opin. Cell Biol.*, 2020, **63**, 174–185.
5 X. Wang, A. M. Bove, G. Simone and B. Ma, *Front. Cell Dev. Biol.*, 2020, **8**, 599281.

6 S. J. Modi and V. M. Kulkarni, *Med. Drug Discovery*, 2019, **2**, 100009.

7 S. R. Silva, K. A. Bowen, P. G. Rychahou, L. N. Jackson, H. L. Weiss, E. Y. Lee, C. M. Townsend Jr and B. M. Evers, *Int. J. Cancer*, 2011, **128**, 1045–1056.

8 N. Nishida, H. Yano, T. Nishida, T. Kamura and M. Kojiro, *Vasc. Health Risk Manage.*, 2006, **2**, 213–219.

9 R. G. Yousef, A. Elwan, I. M. Gobaara, A. B. Mehany, W. M. Eldehna, S. A. El-Metwally, B. A. Alsfouk, E. B. Elkaeed, A. M. Metwaly and I. H. Eissa, *J. Enzyme Inhib. Med. Chem.*, 2022, **37**, 2206–2222.

10 R. G. Yousef, A. Ibrahim, M. M. Khalifa, W. M. Eldehna, I. M. Gobaara, A. B. Mehany, E. B. Elkaeed, A. A. Alsfouk, A. M. Metwaly and I. H. Eissa, *J. Enzyme Inhib. Med. Chem.*, 2022, **37**, 1389–1403.

11 E. B. Elkaeed, R. G. Yousef, H. Elkady, I. M. Gobaara, B. A. Alsfouk, D. Z. Husein, I. M. Ibrahim, A. M. Metwaly and I. H. Eissa, *Molecules*, 2022, **27**, 4606.

12 M. S. Taghour, H. Elkady, W. M. Eldehna, N. M. El-Deeb, A. M. Kenawy, E. B. Elkaeed, A. A. Alsfouk, M. S. Alesawy, A. M. Metwaly and I. H. Eissa, *J. Enzyme Inhib. Med. Chem.*, 2022, **37**, 1903–1917.

13 M. S. Taghour, H. Elkady, W. M. Eldehna, N. El-Deeb, A. M. Kenawy, E. B. Elkaeed, B. A. Alsfouk, M. S. Alesawy, D. Z. Husein and A. M. Metwaly, *PLoS One*, 2022, **17**, e0272362.

14 E. B. Elkaeed, R. G. Yousef, H. Elkady, I. M. Gobaara, A. A. Alsfouk, D. Z. Husein, I. M. Ibrahim, A. M. Metwaly and I. H. Eissa, *Processes*, 2022, **10**, 1391.

15 R. G. Yousef, H. Elkady, E. B. Elkaeed, I. M. Gobaara, H. A. Al-Ghulikah, D. Z. Husein, I. M. Ibrahim, A. M. Metwaly and I. H. Eissa, *Molecules*, 2022, **27**, 7719.

16 M. S. Taghour, H. Elkady, W. M. Eldehna, N. El-Deeb, A. M. Kenawy, A. E. Abd El-Wahab, E. B. Elkaeed, B. A. Alsfouk, A. M. Metwaly and I. H. Eissa, *J. Biomol. Struct. Dyn.*, 2022, 1–16.

17 E. B. Elkaeed, R. G. Yousef, H. Elkady, I. M. Gobaara, A. A. Alsfouk, D. Z. Husein, I. M. Ibrahim, A. M. Metwaly and I. H. Eissa, *Processes*, 2022, **10**, 1391.

18 E. B. Elkaeed, M. S. Taghour, H. A. Mahdy, W. M. Eldehna, N. M. El-Deeb, A. M. Kenawy, B. A. Alsfouk, M. A. Dahab, A. M. Metwaly and I. H. Eissa, *J. Enzyme Inhib. Med. Chem.*, 2022, **37**, 2191–2205.

19 A. T. Mavrova, D. Vuchev, K. Anichina and N. Vassilev, *Eur. J. Med. Chem.*, 2010, **45**, 5856–5861.

20 A. T. Mavrova, S. Dimov, D. Yancheva, M. Rangelov, D. Wesselinova and J. A. Tsenov, *Eur. J. Med. Chem.*, 2016, **123**, 69–79.

21 A. G. Golub, V. G. Bdzhola, N. V. Briukhovetska, A. O. Balanda, O. P. Kukharenko, I. M. Kotey, O. V. Ostrynska and S. M. Yarmoluk, *Eur. J. Med. Chem.*, 2011, **46**, 870–876.

22 S. A. Elmetwally, K. F. Saied, I. H. Eissa and E. B. Elkaeed, *Bioorg. Chem.*, 2019, **88**, 102944.

23 S. A. El-Metwally, M. M. Abou-El-Regal, I. H. Eissa, A. B. Mehany, H. A. Mahdy, H. Elkady, A. Elwan and E. B. Elkaeed, *Bioorg. Chem.*, 2021, **112**, 104947.

24 Y. Dai, Y. Guo, R. R. Frey, Z. Ji, M. L. Curtin, A. A. Ahmed, D. H. Albert, L. Arnold, S. S. Arries and T. Barlozzari, *J. Med. Chem.*, 2005, **48**, 6066–6083.

25 S. A. El-Metwally, A. K. Khalil and W. M. El-Sayed, *Bioorg. Chem.*, 2020, **94**, 103492.

26 H.-Z. Zhang, Z.-L. Zhao and C.-H. Zhou, *Eur. J. Med. Chem.*, 2018, **144**, 444–492.

27 M. A. A. Fathi, A. A. Abd El-Hafeez, D. Abdelhamid, S. H. Abbas, M. M. Montano and M. Abdel-Aziz, *Bioorg. Chem.*, 2019, **84**, 150–163.

28 R. N. Kumar, Y. Poornachandra, P. Nagender, G. S. Kumar, D. K. Swaroop, C. G. Kumar and B. Narsaiah, *Bioorg. Med. Chem. Lett.*, 2016, **26**, 4829–4831.

29 J. Slawinski, K. Szafranski, A. Pogorzelska, B. Zolnowska, A. Kawiak, K. Macur, M. Belka and T. Baczek, *Eur. J. Med. Chem.*, 2017, **132**, 236–248.

30 S. Valente, D. Trisciuoglio, T. De Luca, A. Nebbioso, D. Labella, A. Lenoci, C. Bigogno, G. Dondio, M. Miceli and G. Brosch, *J. Med. Chem.*, 2014, **57**, 6259–6265.

31 Q.-Q. Xie, H.-Z. Xie, J.-X. Ren, L.-L. Li and S.-Y. Yang, *J. Mol. Graphics Modell.*, 2009, **27**, 751–758.

32 K. Lee, K.-W. Jeong, Y. Lee, J. Y. Song, M. S. Kim, G. S. Lee and Y. Kim, *Eur. J. Med. Chem.*, 2010, **45**, 5420–5427.

33 R. N. Eskander and K. S. Tewari, *Gynecol. Oncol.*, 2014, **132**, 496–505.

34 V. A. Machado, D. Peixoto, R. Costa, H. J. Froufe, R. C. Calhelha, R. M. Abreu, I. C. Ferreira, R. Soares and M.-J. R. Queiroz, *Bioorg. Med. Chem.*, 2015, **23**, 6497–6509.

35 Z. Wang, N. Wang, S. Han, D. Wang, S. Mo, L. Yu, H. Huang, K. Tsui, J. Shen and J. Chen, *PLoS One*, 2013, **8**, e68566.

36 J. Dietrich, C. Hulme and L. H. Hurley, *Bioorg. Med. Chem.*, 2010, **18**, 5738–5748.

37 K. Gewald, E. Schinke and H. Böttcher, *Chem. Ber.*, 1966, **99**, 94–100.

38 P. Di Fruscia, E. Zacharioudakis, C. Liu, S. Moniot, S. Laohasinnarong, M. Khongkow, I. F. Harrison, K. Koltsida, C. R. Reynolds and K. Schmidtkunz, *ChemMedChem*, 2015, **10**, 69–82.

39 M. Aruna Kumari, S. Triloknadh, N. Harikrishna, M. Vijjulatha and C. Venkata Rao, *J. Heterocycl. Chem.*, 2017, **54**, 3672–3681.

40 M. Ghorab and S. Abdel Hamide, *Phosphorus Sulfur Silicon Relat. Elem.*, 1995, **106**, 9–20.

41 T. Mosmann, *J. Immunol. Methods*, 1983, **65**, 55–63.

42 K. M. McKinnon, *Curr. Protoc. Immunol.*, 2018, **120**, 5.1.1–5.1.11.

43 A. Adan, G. Alizada, Y. Kiraz, Y. Baran and A. Nalbant, *Crit. Rev. Biotechnol.*, 2017, **37**, 163–176.

44 D. Wlodkowic, J. Skommer and Z. Darzynkiewicz, *Apoptosis: Methods and Protocols*, 2nd edn, 2009, pp. 19–32.

45 N. A. Alsaif, M. A. Dahab, M. M. Alanazi, A. J. Obaidullah, A. A. Al-Mehizia, M. M. Alanazi, S. Aldawas, H. A. Mahdy and H. Elkady, *Bioorg. Chem.*, 2021, **110**, 104807.

46 N. A. Alsaif, M. S. Taghour, M. M. Alanazi, A. J. Obaidullah, A. A. Al-Mehizia, M. M. Alanazi, S. Aldawas, A. Elwan and H. Elkady, *J. Enzyme Inhib. Med. Chem.*, 2021, **36**, 1093–1114.

47 S. A. El-Metwally, A. A. Abuelkhir, H. Elkady, M. S. Taghour, I. M. Ibrahim, D. Z. Husein, A. A. Alsfouk, A. Sultan, A. Ismail and S. Y. Elkhawaga, *Comput. Biol. Chem.*, 2023, 107928.

48 D. Z. Husein, R. Hassanien and M. Khamis, *RSC Adv.*, 2021, **11**, 27027–27041.

49 T. Wang and D. Z. Husein, *Environ. Sci. Pollut. Res.*, 2023, **30**, 8928–8955.

50 M. J. Waring, J. Arrowsmith, A. R. Leach, P. D. Leeson, S. Mandrell, R. M. Owen, G. Pairaudeau, W. D. Pennie, S. D. Pickett and J. Wang, *Nat. Rev. Drug Discovery*, 2015, **14**, 475–486.

51 L. L. Ferreira and A. D. Andricopulo, *Drug discovery today*, 2019, **24**, 1157–1165.

52 S. Kar and J. Leszczynski, *Expert Opin. Drug Discovery*, 2020, **15**, 1473–1487.

53 G. Moroy, V. Y. Martiny, P. Vayer, B. O. Villoutreix and M. A. Miteva, *Drug discovery today*, 2012, **17**, 44–55.

54 A. R. Kotb, D. A. Bakhotmah, A. E. Abdallah, H. Elkady, M. S. Taghour, I. H. Eissa and M. A. El-Zahabi, *RSC Adv.*, 2022, **12**, 33525–33539.

55 A. R. Kotb, A. E. Abdallah, H. Elkady, I. H. Eissa, M. S. Taghour, D. A. Bakhotmah, T. M. Abdelghany and M. A. El-Zahabi, *RSC Adv.*, 2023, **13**, 10488–10502.

56 L. Ma, C. Xie, Y. Ma, J. Liu, M. Xiang, X. Ye, H. Zheng, Z. Chen, Q. Xu and T. Chen, *J. Med. Chem.*, 2011, **54**, 2060–2068.

57 L. Ma, S. Li, H. Zheng, J. Chen, L. Lin, X. Ye, Z. Chen, Q. Xu, T. Chen and J. Yang, *Eur. J. Med. Chem.*, 2011, **46**, 2003–2010.

58 A. Van de Loosdrecht, R. Beelen, g. Ossenkoppele, M. Broekhoven and M. Langenhuijsen, *J. Immunol. Methods*, 1994, **174**, 311–320.

59 M. C. Alley, D. A. Scudiero, A. Monks, M. L. Hursey, M. J. Czerwinski, D. L. Fine, B. J. Abbott, J. G. Mayo, R. H. Shoemaker and M. R. Boyd, *Cancer Res.*, 1988, **48**, 589–601.

60 W. M. Eldehna, M. A. El Hassab, Z. M. Elsayed, T. Al-Warhi, H. Elkady, M. F. Abo-Ashour, M. A. Abourehab, I. H. Eissa and H. A. Abdel-Aziz, *Sci. Rep.*, 2022, **12**, 12821.

61 E. B. Elkaeed, R. G. Yousef, H. Elkady, A. B. Mehany, B. A. Alsfouk, D. Z. Husein, I. M. Ibrahim, A. M. Metwaly and I. H. Eissa, *J. Biomol. Struct. Dyn.*, 2022, 1–16.

62 M. M. Alanazi, H. Elkady, N. A. Alsaif, A. J. Obaidullah, H. M. Alkahtani, M. M. Alanazi, M. A. Alharbi, I. H. Eissa and M. A. Dahab, *RSC Adv.*, 2021, **11**, 30315–30328.

63 M. J. Abraham, T. Murtola, R. Schulz, S. Páll, J. C. Smith, B. Hess and E. Lindahl, *SoftwareX*, 2015, **1**, 19–25.

64 S. Jo, X. Cheng, S. M. Islam, L. Huang, H. Rui, A. Zhu, H. S. Lee, Y. Qi, W. Han and K. Vanommeslaeghe, *Adv. Protein Chem. Struct. Biol.*, 2014, **96**, 235–265.

65 J. Lee, X. Cheng, S. Jo, A. D. MacKerell, J. B. Klauda and W. Im, *Biophys. J.*, 2016, **110**, 641a.

66 T. Tuccinardi, *Expert Opin. Drug Discovery*, 2021, **16**, 1233–1237.

67 M. S. Valdés-Tresanco, M. E. Valdés-Tresanco, P. A. Valiente and E. Moreno, *J. Chem. Theory Comput.*, 2021, **17**, 6281–6291.

68 C. Bouysset and S. Fiorucci, *J. Cheminf.*, 2021, **13**, 1–9.

69 S. Salentin, S. Schreiber, V. J. Haupt, M. F. Adasme and M. Schroeder, *Nucleic Acids Res.*, 2015, **43**, W443–W447.

70 T. Tubiana, J.-C. Carvaillo, Y. Boulard and S. Bressanelli, *J. Chem. Inf. Model.*, 2018, **58**, 2178–2182.

71 A. Amadei, A. B. Linssen and H. J. Berendsen, *Proteins: Struct., Funct., Bioinf.*, 1993, **17**, 412–425.

72 E. Papaleo, P. Mereghetti, P. Fantucci, R. Grandori and L. De Gioia, *J. Mol. Graphics Modell.*, 2009, **27**, 889–899.

73 G. G. Maisuradze and D. M. Leitner, *Proteins: Struct., Funct., Bioinf.*, 2007, **67**, 569–578.

74 B. Hess, *Phys. Rev. E*, 2000, **62**, 8438.

75 E. B. Elkaeed, R. G. Yousef, M. M. Khalifa, A. Ibrahim, A. B. Mehany, I. M. Gobaara, B. A. Alsfouk, W. M. Eldehna, A. M. Metwaly and I. H. Eissa, *Molecules*, 2022, **27**, 6203.

76 H. Elkady, A. Elwan, H. A. El-Mahdy, A. S. Doghish, A. Ismail, M. S. Taghour, E. B. Elkaeed, I. H. Eissa, M. A. Dahab and H. A. Mahdy, *J. Enzyme Inhib. Med. Chem.*, 2022, **37**, 403–416.